https://doi.org/10.5194/egusphere-2026-3294
Preprint. Discussion started: 29 July 2026

ADELM v1.0: a differentiable ecohydrological land model with learnable and diagnosable parameterization

Shijie Jiang[1,2], Georgios Blougouras[1,2], Tuya Wulan[1,3], Yijian Zeng[3], and Jialiang Zhou[1,2]

[1]Department Biogeochemical Integration, Max Planck Institute for Biogeochemistry, Jena, Germany
[2]ELLIS Unit Jena, Jena, Germany
[3]Faculty of Geo-Information Science and Earth Observation, University of Twente, Enschede, The Netherlands

Correspondence: Shijie Jiang (sjiang@bgc-jena.mpg.de)

Abstract. Land surface model (LSM) parameters translate vegetation, soil, snow, and hydrological properties into process controls on water, energy, and carbon exchange. Many of these parameters are not directly measurable at the grid scale, and their effective values depend on model structure, spatial aggregation, and observational constraints. Here we present the Adaptive Differentiable Ecohydrological Land Model (ADELM) v1.0, a fully differentiable LSM that combines process-based equations with machine learning, allowing each parameter to be prescribed or learned from observations and making parameterization itself a learnable and diagnosable part of the land model. ADELM couples canopy radiative transfer, soil hydraulics, photosynthesis, evapotranspiration, and snow and soil hydrology within a single automatic-differentiation graph, so that selected parameters can be learned directly from observed fluxes or states. Because a learned parameter can be expressed as a function of gridded environmental attributes, mappings trained at sparse sites can be applied across continuous spatial domains. We demonstrate ADELM in a European application using evapotranspiration and gross primary productivity constraints from eddy covariance sites. Mappings learned at the sites are evaluated across the 0.1° European grid, where observation-constrained learning improves evapotranspiration simulation and produces spatially coherent flux and parameter fields. Greater parameter flexibility can leave the learned parameters less identifiable, so learned parameterizations need to be judged by the stability and coherence of their parameter fields. Overall, ADELM provides a differentiable foundation for developing parameterizations that can be learned from observations, applied across space, and diagnosed for reliability.

1 Introduction

Land surface models (LSMs) simulate terrestrial exchanges of water, energy, and carbon in response to climate, rising CO_2, and land-use change, and they provide the land component through which Earth system models project the carbon sink and land-climate feedbacks (Blyth et al., 2021; Fisher and Koven, 2020). The credibility of those projections depends on both the represented processes and the parameters that control them. Parametric uncertainty is a leading source of spread in projected land carbon and water states (Booth et al., 2012; Fisher et al., 2019). Parameters enter an LSM through its parameterizations, the functions that map vegetation, soil, climate, and topography to the process controls behind simulated exchanges of water, energy, carbon, and biogeochemical processes (Raoult et al., 2025). In most LSMs, these parameters are assigned before

https://doi.org/10.5194/egusphere-2026-3294
Preprint. Discussion started: 29 July 2026

simulation through fixed constants, plant-functional-type (PFT) lookup tables, and pedotransfer functions, and are seldom revised once the model equations are set (Margiotta et al., 2026; Verhoef et al., 2026).

In practice, however, many of these parameters cannot be measured directly at the model's scale. For example, vegetation parameters are typically informed by observations on a limited number of species and locations, and can vary substantially with local and seasonal conditions (Massoud et al., 2019), and soil hydraulic relationships are similarly derived from cores or laboratory samples. Once transferred to a grid cell, such values become effective parameters. They absorb local vegetation and soil properties, sub-grid heterogeneity, nonlinear process aggregation, and structural assumptions in the model, so the grid-scale values of these parameters that best reproduce observed fluxes can differ from lab measurements, pedotransfer estimates, or PFT lookup values (Cranko Page et al., 2023; Weber et al., 2024). Inferring these effective parameters from observations is itself an established line of work (Keetz et al., 2025; Kumar et al., 2022). Bayesian calibration, gradient-free optimization, and sequential and variational data assimilation have all been applied to land surface and ecosystem models with considerable site-level success (Kaminski and Mathieu, 2017; Kuppel et al., 2012; MacBean et al., 2022). Extending them across space is harder, since parameters fitted at one location do not in general transfer to another (Bastrikov et al., 2018; Beck et al., 2016), and exploring the high-dimensional, coupled parameter space of an LSM is computationally costly when repeated across many grid cells (Keetz et al., 2025; Tang et al., 2025).

Parameter regionalization addresses this problem by transferring parameter information from observed locations to unobserved locations using relationships between model parameters and environmental descriptors, such as soil texture, topography, vegetation cover, groundwater depth, and long-term climate (Merz and Blöschl, 2004; Parajka et al., 2005; Samaniego et al., 2010; Beck et al., 2020). In traditional implementations, parameter estimation and spatial transfer are often treated as sequential steps. In particular, parameters are first calibrated at individual sites or gauged basins and then regionalized through transfer rules based on spatial proximity, physical similarity, regression, or machine-learning methods (Heuvelmans et al., 2006; Feigl et al., 2022). More recently, hybrid and differentiable modeling frameworks, which embed machine-learning components within process-based equations, have offered a way to merge these steps by optimizing the attribute-to-parameter mapping and the process model jointly against observations (Reichstein et al., 2019; Tsai et al., 2021; Shen et al., 2023). For gradient-based end-to-end training, the relevant process equations must be implemented in a differentiable form. Automatic differentiation can then propagate observational loss backward through the same dependencies used in the forward simulation, so updates to the attribute-to-parameter mapping depend on how its predicted parameters can alter simulated states and fluxes. Importantly, observations can then directly constrain the parameterization that generates the simulated response (Jiang et al., 2020; Bao et al., 2023; Koppa et al., 2022).

Examples of this framework have grown rapidly across hydrology and land modeling (Chen et al., 2023; Gelbrecht et al., 2023). For example, at the catchment scale, differentiable hydrological models learn a mapping from static catchment attributes (such as climate, soil, and topography) to the parameters of a process-based hydrological model (Feng et al., 2022; Colleoni et al., 2025). Because this mapping is shared across catchments, observations from many basins jointly constrain it, allowing parameters to be transferred to catchments that were not individually calibrated. Recent land-modeling studies have reimplemented process models in differentiable frameworks or embedded neural parameterizations within land components, such as

https://doi.org/10.5194/egusphere-2026-3294
Preprint. Discussion started: 29 July 2026

JAX-CanVeg (Jiang et al., 2025), NoahPy (Tian et al., 2026), ClimaLand (Deck et al., 2026), and DifferLand (Fang et al., 2026). These advances show that differentiable modeling can learn parameterizations from observations within models that retain a physical backbone. In these frameworks, however, the choice of which parameters to learn, in what form, and under which observational constraints is typically fixed when the model is built. Subsequent studies therefore evaluate the consequences of this pre-specified choice (e.g., Fang and Gentine, 2024). Parameterization itself is thus not yet treated as a testable component of the model: there is no systematic, parameter-by-parameter framework for asking whether a quantity conventionally prescribed from prior knowledge would be better learned from observations.

Here we introduce the Adaptive Differentiable Ecohydrological Land Model (ADELM) v1.0, a process-based LSM in which the assignment of each parameter is treated as an explicit modeling choice within a differentiable architecture. ADELM represents the coupled water, energy, and carbon exchange of the land surface, with its process equations, parameter mappings, prognostic state updates, and loss function sharing a single automatic-differentiation graph. Errors in simulated fluxes or states (compared with observations) therefore constrain selected parameters through the same coupled pathways that generate the model outputs. The source of each parameter is itself a choice among a prescribed value, a globally shared learned value, or a spatially varying value learned as a function of environmental attributes defined across the domain. This spatial function plays the same role as a conventional attribute-to-parameter relationship (such as a pedotransfer function), but its form is learned from observations and can be any differentiable function, from a simple parametric form to a neural network. Holding the process equations fixed while varying only these choices makes ADELM a controlled testbed for parameterization, in which whether and how each parameter should be learned becomes an explicit object of investigation. It may thereby open a way to revisit parameters that LSMs have long prescribed, and to let observations reveal new, more informative expressions for them.

We demonstrate ADELM over Europe using eddy covariance observations of evapotranspiration (ET) and gross primary productivity (GPP). These observations constrain the attribute-to-parameter mappings at the grid cells that contain flux sites. Because each learned mapping is a function of environmental attributes that are defined everywhere, it can then be evaluated across the full domain to produce spatially continuous parameter and flux fields. Within this setup, we compare four configurations, i.e., a prescribed baseline, a vegetation-focused learned parameterization, a soil- and snow-focused learned parameterization, and a combined learned parameterization. We evaluate how these choices affect held-out site-level flux skill, gridded ET and GPP patterns, learned parameter fields, and parameter identifiability. The study aims to answer (1) whether parameter mappings trained at sparse, clustered flux sites remain reliable when applied across the full gridded domain, and (2) how the choice of what to learn shapes both the resulting flux skill and the identifiability of the learned parameters.

The remainder of this paper is organized as follows. Sect. 2 describes ADELM's overall architecture and implementation, including the coupled ecohydrological processes, the parameterization system, and the computational infrastructure that ties these together. Sections 3 and 4 demonstrate ADELM with a European case study, followed by discussions in Sect. 5.

https://doi.org/10.5194/egusphere-2026-3294
Preprint. Discussion started: 29 July 2026

2 Overall model architecture and implementation

ADELM is an LSM implemented in a differentiable programming framework, projecting atmospheric forcings and static environmental attributes onto daily fields of land-surface fluxes and prognostic states. The model contains two connected but modular components (Fig. 1). The first is a process-based ecohydrological core that advances the coupled water, energy, and carbon exchange through time; the second is a configurable parameterization system that supplies the parameter values entering the process equations. The same process core runs unchanged whether a given parameter is prescribed or learned, and the source of each parameter can be reconfigured through the model configuration without modifying the model code.

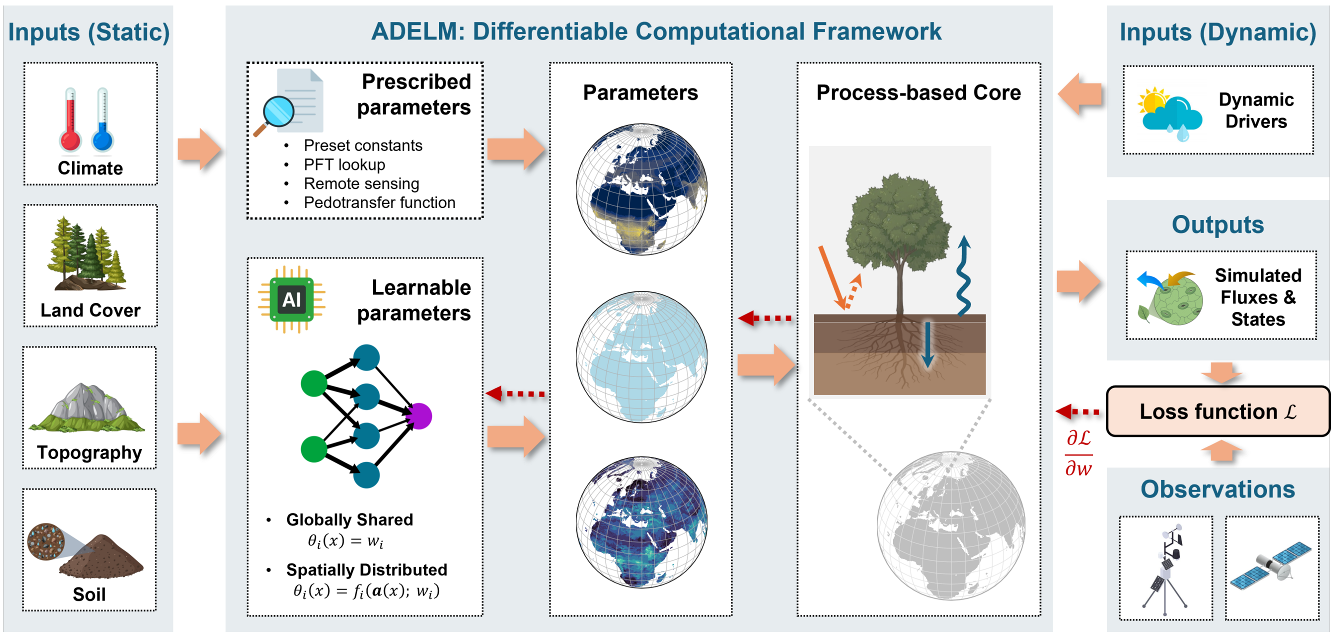

Figure 1. The computational framework of the Adaptive Differentiable Ecohydrological Land Model (ADELM). Static environmental attributes (e.g., climate, land cover, topography, soil) and dynamic drivers (e.g., meteorology, leaf area index, atmospheric CO_2) are the model inputs. The source of each process parameter is declared in the model configuration, and can be prescribed (from preset constants, plant-functional-type lookup, remote sensing, or pedotransfer functions) or learned. Learned parameters take one of two forms, a globally shared value ($\Theta_i = w_i$) or a spatially distributed function of static attributes ($\Theta_i(x) = f_i(\boldsymbol{a}(x); w_i)$). The three globes in the central column show schematic example parameter fields produced under each source over a generic global domain: a prescribed parameter (top), a globally shared learned parameter that takes a single value everywhere (middle), and a spatially distributed learned parameter (bottom); the global domain is illustrative, as the parameterization is not tied to any particular region or scale. Regardless of source, parameters enter the same process-based ecohydrological core, which is driven forward to produce simulated fluxes and states. When observations are available, a loss function compares simulated and observed variables, and gradients are propagated back through the coupled core to the learnable parameters and mapping weights ($\partial\mathcal{L}/\partial w$).

https://doi.org/10.5194/egusphere-2026-3294
Preprint. Discussion started: 29 July 2026

2.1 Forward simulation

Let Ω denote the spatial domain, $x \in \Omega$ a spatial unit (e.g., a grid cell), and t the daily time index. Given the static environmental attributes $\boldsymbol{a}(x)$, the dynamic drivers $\boldsymbol{F}(x,t)$ (as listed in Table 1), and a parameter set $\boldsymbol{\Theta}(x)$, the forward operator $\mathcal{M}$ advances the prognostic state $\boldsymbol{s}(x,t)$ and produces the simulated diagnostic fluxes $\hat{\boldsymbol{y}}(x,t)$, as

$$\boldsymbol{s}(x,t+1),\, \hat{\boldsymbol{y}}(x,t) = \mathcal{M}\big(\boldsymbol{s}(x,t),\, \boldsymbol{F}(x,t);\, \boldsymbol{\Theta}(x)\big). \tag{1}$$

The state vector $\boldsymbol{s}(x,t)$ collects soil water storage across multiple layers, snow water storage, and canopy interception storage. The flux vector $\hat{\boldsymbol{y}}(x,t)$ contains water, carbon, and energy fluxes, such as ET, GPP, runoff, and snowmelt, at daily resolution. The static attributes $\boldsymbol{a}(x)$ include long-term climate, land cover, topography, and soil texture, all defined across Ω from data products (Sect. 3). They enter $\mathcal{M}$ through the parameter set $\boldsymbol{\Theta}(x)$, which is either prescribed or learned as a function of $\boldsymbol{a}(x)$ (Sect. 2.2).

Table 1. Time-varying drivers of the ADELM v1.0 process core.

Variable	Units	Description
T_{a}	$^{\circ}\mathrm{C}$	Near-surface air temperature
$T_{\mathrm{a,min}}$	$^{\circ}\mathrm{C}$	Daily minimum air temperature
$T_{\mathrm{a,max}}$	$^{\circ}\mathrm{C}$	Daily maximum air temperature
P	$\mathrm{mm\,d^{-1}}$	Daily precipitation (liquid-water equivalent)
$R_{\mathrm{sw}}^{\downarrow}$	$\mathrm{W\,m^{-2}}$	Downward shortwave radiation
$R_{\mathrm{lw}}^{\downarrow}$	$\mathrm{W\,m^{-2}}$	Downward longwave radiation
u	$\mathrm{m\,s^{-1}}$	Wind speed at reference height
VPD	kPa	Vapour pressure deficit
LAI	$\mathrm{m^2\,m^{-2}}$	Leaf area index
C_{a}	ppm	Atmospheric CO_2 concentration

The forward operator $\mathcal{M}$ is obtained by composition of five process modules (Fig. 2), written compactly as

$$\mathcal{M} = \mathcal{M}_{\mathrm{wb}} \circ \mathcal{M}_{\mathrm{et}} \circ \mathcal{M}_{\mathrm{photo}} \circ \mathcal{M}_{\mathrm{hydra}} \circ \mathcal{M}_{\mathrm{rad}}. \tag{2}$$

where $\mathcal{M}_{\mathrm{rad}}$, $\mathcal{M}_{\mathrm{hydra}}$, $\mathcal{M}_{\mathrm{photo}}$, $\mathcal{M}_{\mathrm{et}}$, $\mathcal{M}_{\mathrm{wb}}$ are modules for radiative transfer, soil hydraulics, photosynthesis, evapotranspiration, and snow and soil water balance, respectively. The symbol $\circ$ denotes sequential application within each daily time step, from radiative transfer to snow and soil water balance, which closes the step by updating the prognostic state for the next day (Fig. 2). Each module is briefly described below, with full equations in Appendix A.

The radiative transfer module $\mathcal{M}_{\mathrm{rad}}$ partitions incoming shortwave and longwave radiation between the vegetation canopy and the ground surface and computes the net energy absorbed by each. Shortwave radiation is treated with a two-stream canopy scheme (Sellers, 1985; Dickinson, 1983) that resolves visible and near-infrared bands and their direct-beam and diffuse

https://doi.org/10.5194/egusphere-2026-3294
Preprint. Discussion started: 29 July 2026

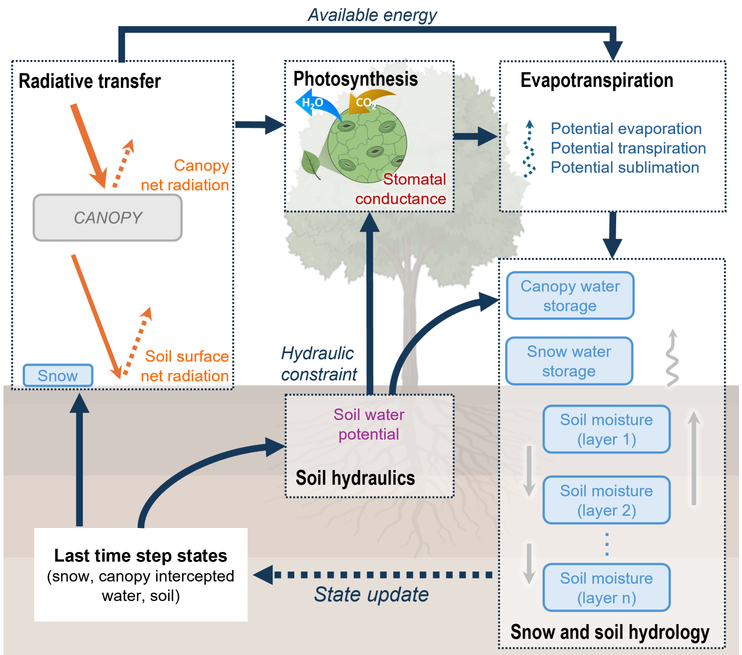

Figure 2. Coupled ecohydrological process representation in ADELM. The five process modules of $\mathcal{M}$ (see Eq. (2)) are shown as dashed boxes. Solid arrows indicate the main forward coupling pathways between modules, labelled with the principal variable transmitted along each pathway. The dashed arrow at the bottom indicates the prognostic state update from one time step to the next.

components. Longwave radiation is treated as broadband thermal exchange among atmosphere, canopy, and ground. The net radiation absorbed by vegetation and ground combines the two contributions,

$$R_{\mathrm{n,v}} = R^{\mathrm{n}}_{\mathrm{sw,v}} + R^{\mathrm{n}}_{\mathrm{lw,v}}, \qquad R_{\mathrm{n,g}} = R^{\mathrm{n}}_{\mathrm{sw,g}} + R^{\mathrm{n}}_{\mathrm{lw,g}}, \tag{3}$$

where subscripts v and g denote the vegetation canopy and the ground surface, $R^{\mathrm{n}}_{\mathrm{sw}}$ is the net absorbed shortwave radiation summed over the visible and near-infrared bands, and $R^{\mathrm{n}}_{\mathrm{lw}}$ is the net absorbed longwave radiation. The net radiation terms $R_{\mathrm{n,v}}$ and $R_{\mathrm{n,g}}$ are passed to the evapotranspiration module. The visible-band component of canopy net absorption is converted to absorbed photosynthetically active radiation $\mathrm{APAR}_{\mathrm{leaf}}$ for the photosynthesis module. Full derivations of the two-stream coefficients and the longwave exchange terms are in Appendix A1.

The hydraulics module $\mathcal{M}_{\mathrm{hydra}}$ diagnoses how the current soil moisture state constrains plant water supply. It represents plant water access with a prescribed vertical root distribution and a minimum leaf water potential $\psi_{\mathrm{leaf,min}}$, and returns two outputs to downstream modules: layer-wise root water uptake fractions ζ_i used by the snow and soil hydrology module to distribute transpiration withdrawals, and a root-zone soil water potential ψ_{root} that enters the stomatal regulation of photosynthesis. For each soil layer, the potential plant water supply combines the root fraction in that layer, a layer-specific hydraulic

https://doi.org/10.5194/egusphere-2026-3294
Preprint. Discussion started: 29 July 2026

conductivity, and the soil-to-leaf water potential gradient,

$$S_i = f_{\mathrm{root},i}\, K_i \,\max\!\left(\psi_{\mathrm{soil},i} - \psi_{\mathrm{leaf,min}}, 0\right), \tag{4}$$

where $f_{\mathrm{root},i}$ is the root fraction in layer i, K_i is the hydraulic conductivity diagnosed from the current soil moisture through a power-law relationship (Campbell, 1974), and $\psi_{\mathrm{soil},i}$ is the soil water potential diagnosed from a modified Campbell retention curve with a linear interpolation between field capacity and saturation. The root-zone potential passed to photosynthesis is the supply-weighted average $\psi_{\mathrm{root}} = \sum_i \zeta_i\, \psi_{\mathrm{soil},i}$, with $\zeta_i = S_i / \sum_j S_j$ the normalized layer-wise uptake fractions. Root profile, retention curve, and conductivity functions are detailed in Appendix A2.

The photosynthesis module $\mathcal{M}_{\mathrm{photo}}$ estimates daily canopy-scale GPP from absorbed PAR, atmospheric CO_2, air temperature, canopy conductance, and root-zone water status. ADELM v1.0 uses a compact big-leaf formulation (Knauer et al., 2018) in which GPP follows a smooth co-limitation between a light-limited uptake rate A_{l} and a diffusion-limited uptake rate A_{d} (Collatz et al., 1991; Sellers et al., 1992), expressed as the smaller positive root of

$$\theta_{\mathrm{co}}\, \mathrm{GPP}^2 - (A_{\mathrm{l}} + A_{\mathrm{d}})\, \mathrm{GPP} + A_{\mathrm{l}} A_{\mathrm{d}} = 0, \tag{5}$$

where θ_{co} is a curvature parameter, $A_{\mathrm{l}} = \epsilon_{\mathrm{L}}\, \mathrm{APAR}_{\mathrm{leaf}}$ is light-limited with light-use efficiency ϵ_{L}, and $A_{\mathrm{d}} = g_{\mathrm{c,CO_2}}(C_{\mathrm{a}} - C_{\mathrm{i,can}})$ is diffusion-limited. The canopy CO_2 conductance $g_{\mathrm{c,CO_2}}$ combines stomatal, leaf boundary-layer, and above-canopy aerodynamic conductances in series, with stomatal regulation given by a Jarvis multiplicative scheme (Jarvis, 1976) driven by radiation, temperature, vapor pressure deficit, and ψ_{root}. The internal canopy CO_2 concentration $C_{\mathrm{i,can}}$ is diagnosed by equating diffusive CO_2 supply with a Farquhar-type capacity (Farquhar et al., 1980). Full forms of the Jarvis factors, the Farquhar capacity equation, and the resistance network are given in Appendix A3.

The evapotranspiration module $\mathcal{M}_{\mathrm{et}}$ estimates daily potential rates of canopy transpiration, soil evaporation, snow sublimation, and wet-canopy evaporation through Penman–Monteith-type formulations (Monteith, 1965). Each pathway $j \in \{\mathrm{tr}, \mathrm{soil}, \mathrm{can\text{-}liq}, \mathrm{sub}, \mathrm{snow}\}$ follows the canonical Penman–Monteith form

$$E_{j,\mathrm{pot}} = \frac{\Delta_j\, R_{\mathrm{n},j} + \rho_{\mathrm{a}} c_p\, \Delta e_j / r_{\mathrm{a},j}}{\lambda_j \left[\Delta_j + \gamma_j \left(1 + r_{\mathrm{s},j}/r_{\mathrm{a},j}\right)\right]}, \tag{6}$$

where $R_{\mathrm{n},j}$ is the net radiation at the relevant surface (canopy for $j \in \{\mathrm{tr}, \mathrm{can\text{-}liq}, \mathrm{sub}\}$ and ground for $j \in \{\mathrm{soil}, \mathrm{snow}\}$), $r_{\mathrm{a},j}$ is the aerodynamic resistance from the surface to the reference height, $r_{\mathrm{s},j}$ is the surface resistance (canopy stomatal resistance for transpiration, soil surface resistance for soil evaporation, and zero for wet-canopy and snow pathways), Δe_j is the surface-to-air vapor pressure deficit, ρ_{a} is air density, c_p is the specific heat of air, and $(\Delta_j, \lambda_j, \gamma_j)$ are the saturation vapor pressure slope, latent heat, and psychrometric constant evaluated with liquid-phase quantities for $j \in \{\mathrm{tr}, \mathrm{soil}, \mathrm{can\text{-}liq}\}$ and with their ice-phase counterparts for $j \in \{\mathrm{sub}, \mathrm{snow}\}$. The canopy stomatal resistance entering the transpiration pathway is derived from $g_{\mathrm{s,can}}$ in the photosynthesis module. These demand-driven potential rates are converted to actual fluxes in the snow and soil hydrology module $\mathcal{M}_{\mathrm{wb}}$, where each is capped by the available water. Full forms of the five sets of resistances, the surface-to-air vapor pressure gradients, and the ice-phase substitutions are in Appendix A4.

The snow and soil hydrology module $\mathcal{M}_{\mathrm{wb}}$ closes the daily water balance for canopy interception, ground snow, and the multi-layer soil column. Precipitation is first partitioned into rainfall and snowfall using a temperature-dependent warm-day

https://doi.org/10.5194/egusphere-2026-3294
Preprint. Discussion started: 29 July 2026

fraction. Liquid canopy interception ($W_{\text{can,liq}}$), intercepted snow ($W_{\text{can,sol}}$), and ground snow (W_{snow}) are tracked as separate bucket-type stores,

$$W^{t+1}_{\text{can,liq}} = W^{t}_{\text{can,liq}} + I_{\text{can,liq}} - D_{\text{can,liq}} - E_{\text{can,liq}}, \tag{7}$$

$$W^{t+1}_{\text{can,sol}} = W^{t}_{\text{can,sol}} + I_{\text{can,sol}} - D_{\text{can,sol}} - E_{\text{sub}}, \tag{8}$$

$$W^{t+1}_{\text{snow}} = W^{t}_{\text{snow}} + P_{\text{snow}} + D_{\text{can,sol}} - M - E_{\text{snow}}, \tag{9}$$

where $I_{\text{can,liq}}$ and $I_{\text{can,sol}}$ are the liquid and solid canopy interception inputs, $D_{\text{can,liq}}$ and $D_{\text{can,sol}}$ are drip from the wet canopy and snow falloff from the canopy to the ground, P_{snow} is the snowfall reaching the ground, and M is snowmelt. Soil water in each layer is updated by mass conservation,

$$\theta^{t+1}_{i} = \theta^{t}_{i} + \frac{\Delta t}{\Delta z_i}\big(Q_{i-1} - Q_i - \zeta_i\, E_{\text{tr}} - \delta_{i1}\, E_{\text{soil}}\big), \tag{10}$$

where θ_i is the volumetric water content of layer i, Q_{i-1} and Q_i are the water fluxes at the upper and lower interfaces of layer i, $\zeta_i E_{\text{tr}}$ is transpiration withdrawal using the uptake fractions from the hydraulics module, $\delta_{i1} E_{\text{soil}}$ restricts soil evaporation to the top layer, Δz_i is the layer thickness, and Δt is the daily time step. The module also limits the potential ET demands from $\mathcal{M}_{\text{et}}$ to the water available in each store, generates drainage from the bottom soil layer, and produces surface runoff when infiltration capacity is exceeded. The updated bucket and soil states together form the prognostic state vector $\boldsymbol{s}(x, t+1)$ returned to the forward simulation. Full forms of the interception partitioning, drip and falloff rules, snowmelt scheme, and drainage parameterization are in Appendix A5.

2.2 Parameterization system and learning algorithm

The parameterization system assembles the parameter set $\boldsymbol{\Theta}(x)$ from individual parameters, with the source of each parameter declared separately in the model configuration. Three sources are available, i.e., a prescribed value, a globally shared learned value, and a spatially varying learned function of the environmental attributes $\boldsymbol{a}(x)$. Because each parameter declares its source independently, prescribed and learned parameters can be combined freely within one simulation, and the same model can be reconfigured between runs by changing only these declarations.

A prescribed parameter is set in advance from a fixed constant, a plant-functional-type (PFT) lookup table, a remote-sensing product, or a pedotransfer function, which are the conventional sources used in an LSM. A globally shared learned parameter takes a single value w_i applied at every location,

$$\Theta_i(x) = w_i, \tag{11}$$

where the subscript i indexes an individual process parameter. A spatially varying learned parameter is a function of the static attributes,

$$\Theta_i(x) = f_i\big(\boldsymbol{a}(x); w_i\big), \tag{12}$$

https://doi.org/10.5194/egusphere-2026-3294
Preprint. Discussion started: 29 July 2026

where w_i are the learnable weights of f_i. Because the model is differentiable end to end, f_i can be any differentiable mapping of the attributes, whether an alternative neural architecture or a differentiable parametric or equation-based form; in this work it is a small multilayer perceptron (MLP) with its own weights per parameter. The MLPs share a common architecture, e.g., a fixed set of input attributes and hidden-layer widths, declared once in the configuration. Evaluated at every grid cell, f_i produces a parameter field at the resolution of the simulation grid. The mapping f_i serves the same role as a pedotransfer or attribute-to-parameter function, with the difference that its form is learned from observations.

Each learned parameter, whether shared or spatially varying, is optimized as a quantity z_i and mapped to its physical range by a smooth bounded transform,

$$\Theta_i = \Theta_i^{\min} + \left(\Theta_i^{\max} - \Theta_i^{\min}\right) \ell(z_i), \tag{13}$$

where $\ell(z) = 1/(1+e^{-z})$ is the logistic function and $\Theta_i^{\min}$, $\Theta_i^{\max}$ are physical bounds declared for that parameter. The transform holds each learned parameter inside its physically meaningful range throughout training. The choice of input attributes, hidden-layer widths, and physical bounds for the European application is given in Sect. 3.

When observations are available, selected simulated variables are compared with their observed counterparts through a loss function

$$\mathcal{L} = \sum_k \alpha_k \, \mathcal{L}_k\big(\hat{\boldsymbol{y}}_k, \boldsymbol{y}_k^{\mathrm{obs}}\big), \tag{14}$$

where k indexes the variables that enter the loss, for example daily ET, GPP, or soil moisture, α_k are scalar weights, $\hat{\boldsymbol{y}}_k$ and $\boldsymbol{y}_k^{\mathrm{obs}}$ are the collections of simulated and observed values for variable k across the training sites and times, and $\mathcal{L}_k$ is a per-variable loss, such as a Nash–Sutcliffe efficiency (NSE) score (Nash and Sutcliffe, 1970), that aggregates these values in a specified way. The same form applies to single-site and multi-site learning, and to single-variable and multi-variable constraints.

The optimization problem is to find the learnable parameters w, i.e., the shared values and MLP weights introduced in Sect. 2.2, that minimize $\mathcal{L}$ for the given observations,

$$\hat{w} = \arg\min_w \mathcal{L}\big(\hat{\boldsymbol{y}}(w), \boldsymbol{y}^{\mathrm{obs}}\big), \tag{15}$$

where $\hat{\boldsymbol{y}}(w) = \mathcal{M}\big(\cdot\,; \boldsymbol{\Theta}(w)\big)$ denotes the simulated output obtained by running the forward model with the parameter set supplied by the parameterization system. Because the entire chain, comprising the process modules, the prognostic state updates, the parameterization mappings, and the loss, sits within a single automatic-differentiation graph, the gradient $\partial\mathcal{L}/\partial w$ is obtained by backpropagation through the same coupled calculations that generated the simulation, using the PyTorch automatic-differentiation backend (Paszke et al., 2019). The parameters are updated with the Adam optimizer (Kingma and Ba, 2014); the learning rate schedule and stopping criteria adopted for the European application are described in Sect. 3.

The model configuration specifies which simulated variables enter $\mathcal{L}$ and which parameters carry learnable weights, so that different observations can constrain different parameters within the same simulation. Because a learned mapping f_i depends only on static attributes that are defined everywhere across Ω, a mapping fitted at locations where observations are available can be evaluated over the full domain to produce spatially continuous parameter and flux fields.

https://doi.org/10.5194/egusphere-2026-3294
Preprint. Discussion started: 29 July 2026

2.3 Computational implementation

ADELM v1.0 is implemented as a Python package built on the PyTorch automatic differentiation framework (Paszke et al., 2019). The package is structured as a configurable framework in which the learnable parameters and the observations used to constrain them are specified through a shared configuration file. The file is parsed at startup, so that different experimental setups can be assembled by changing configuration fields without modifying source code. The package is organized into three top-level subsystems, i.e., the process system, the parameterization system, and the runtime system (Fig. 3).

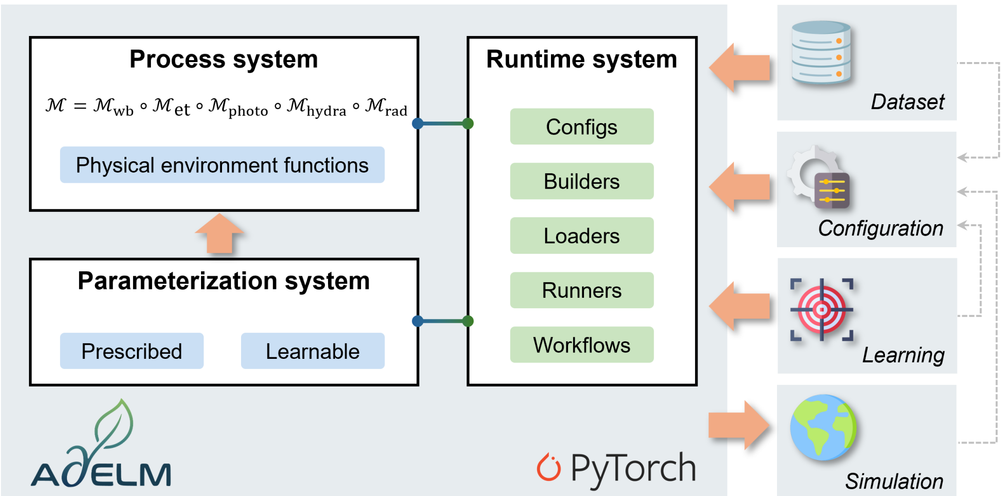

Figure 3. Computational architecture of ADELM. The three internal subsystems are shown within the package on the left, and the external interfaces on the right. Orange arrows mark data flow between the package and these interfaces. Lines connecting internal subsystems mark runtime invocation.

The process system contains the five process modules corresponding to $\mathcal{M}_{\mathrm{rad}}$, $\mathcal{M}_{\mathrm{hydra}}$, $\mathcal{M}_{\mathrm{photo}}$, $\mathcal{M}_{\mathrm{et}}$, and $\mathcal{M}_{\mathrm{wb}}$ of Sect. 2.1, together with shared physical environment functions such as solar geometry, optical properties, pedotransfer functions, and surface exchange coefficients that the process modules call. A central variable registry organizes all model quantities into drivers, states, fluxes, parameters, constants, diagnostics, and balance errors.

The parameterization subsystem implements the three parameter sources declared in Sect. 2.2. A prescribed value is declared as a fixed scalar in the configuration, drawn from a PFT-indexed look-up table, read from a spatially varying data product such as a remote-sensing parameter, or derived from other prescribed quantities through physics routines such as pedotransfer functions. A learned value, by contrast, is trainable. A globally shared value is stored as a single trainable scalar, and a spatially varying value as an independent MLP that maps the static attributes $\boldsymbol{a}(x)$ to the parameter, both kept within their declared physical bounds by a logistic transform. Because the three sources expose the same interface, the process modules consume a parameter identically regardless of its source, so switching a parameter between them is a configuration change that leaves the process code untouched.

https://doi.org/10.5194/egusphere-2026-3294
Preprint. Discussion started: 29 July 2026

The runtime system translates a declarative YAML configuration into a running experiment. It is organized into five subsystems. (1) Configs are organized as a hierarchy of Python dataclasses specifying the soil column discretization, the source declaration for each model parameter, the input file paths and variable name mappings, the optimizer and training schedule, and the cross-validation protocol. (2) Builders are objects that assemble a runnable model instance from a configuration, with a top-level system builder coordinating three subordinate builders that initialize model containers and prognostic state tensors, construct the process chain from the selected process modules, and instantiate the parameterization modules corresponding to the declared parameter sources. (3) Loaders ingest data for two input geometries. The site loader reads site-indexed NetCDF files containing time-varying meteorological drivers, static site attributes, parameter fields, PFT cover fractions, and observation targets. The grid loader reads spatially gridded NetCDF files for large-scale forward simulation. (4) Runners provide three execution entry points. The site learning runner performs gradient-based parameter optimization over a multi-site observation dataset. The site simulation runner performs a forward pass at site scale with fixed or externally supplied parameters. The grid simulation runner executes the forward model over a spatial domain, stepping through driver files and writing model state checkpoints at the end of each month. (5) Workflows structure parameter learning around one of three cross-validation protocols. The no-cross-validation protocol trains over the full site dataset. The spatial cross-validation protocol partitions sites into training and held-out folds with either random or predefined geographic assignment. The temporal cross-validation protocol partitions the time axis into training and held-out periods.

Overall, these subsystems support three end-to-end schemes, namely site-level parameter training, site-level forward simulation, and grid-level forward simulation. The simulated variables that enter the loss, the parameters that carry learnable weights, and the cross-validation protocol are all declared in the configuration. Once a parameterization has been trained, the learned mapping can be frozen and loaded into a subsequent simulation. Alternatively, when all parameters are declared as prescribed sources, the neural components are absent from the forward pass and ADELM operates as a standard LSM at site or grid scale. ADELM is released as open source, with the source code hosted at https://github.com/hydroshub/adelm and technical documentation at https://adelm.org/.

The European application in the following sections demonstrates the three schemes under spatial cross-validation, with experimental variants assembled by composing configuration files through the inheritance mechanism so that each variant overrides only the fields that distinguish it from the baseline.

3 Experimental design

3.1 Data and study setup

This section presents a European-scale illustration of the ADELM framework, configured as a process-based LSM with an observation-constrained parameterization layer. The illustration exercises the three schemes of Sect. 2.3, uses eddy covariance ET and GPP as observational constraints, and evaluates the resulting parameterizations under spatial cross-validation. The European domain is defined as 35–72° N and 12° W–50° E, with forcing data and static attributes prepared on a common 0.1° latitude–longitude grid. The soil column is here discretized into six layers with thicknesses of 0.10, 0.20, 0.30, 0.50, 0.80, and

https://doi.org/10.5194/egusphere-2026-3294
Preprint. Discussion started: 29 July 2026

1.10 m, with surface runoff generated over the upper three layers. Model training and held-out evaluation cover 2001–2020 at a daily time step, with the year 2000 cycled times to spin up the state before each training or evaluation run. During training and spatial cross-validation, ADELM is run for the grid cells containing flux sites (Fig. 4), and the learned attribute-to-parameter mappings are then evaluated over all land grid cells in the domain.

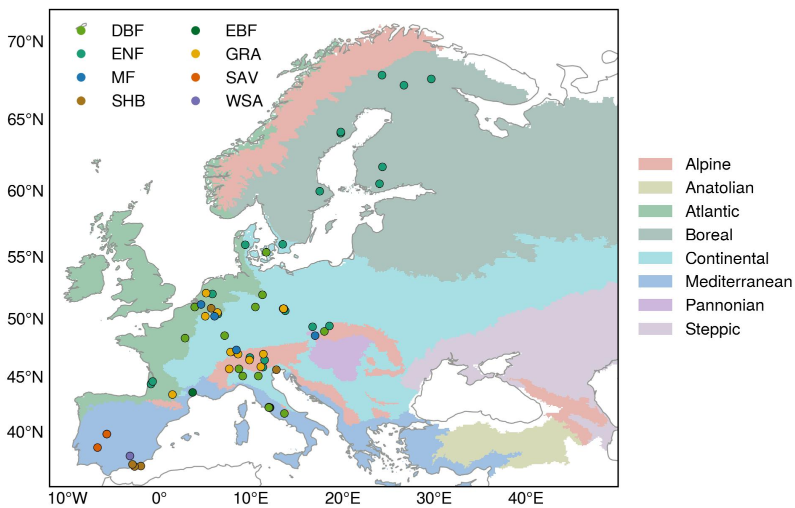

Figure 4. Locations of eddy covariance sites used for model training and evaluation. Point colors indicate plant functional type following the IGBP classification (CSH: closed shrubland; DBF: deciduous broadleaf forest; EBF: evergreen broadleaf forest; ENF: evergreen needleleaf forest; GRA: grassland; MF: mixed forest; OSH: open shrubland; SAV: savanna; WSA: woody savanna). Background colors indicate the biogeographical regions of Europe defined by the European Environment Agency, which are used for regional flux analysis in Sect. 4.2.

Site-level observational constraints are derived from daily eddy covariance records in the PLUMBER2 dataset (Ukkola et al., 2022), the ICOS Warm Winter 2020 collection (Warm Winter 2020 Team and ICOS Ecosystem Thematic Centre, 2020), and the ICOS Drought-2018 collection (Drought 2018 Team and ICOS Ecosystem Thematic Centre, 2020). Sites are restricted to the European domain and screened to retain natural or semi-natural vegetation classes, and are excluded if post-2000 gridded forcing or LAI is missing or if the LAI record contains prolonged artificial zero periods. The final natural-site subset contains 63 sites (Fig. 4; listed in Appendix B). Flux data are processed using FluxnetLSM (Ukkola et al., 2017) for quality filtering, gap filling, unit conversion, and aggregation to daily resolution, and daily flux values are retained only when the quality-control fraction is at least 0.7. ET is derived from latent heat flux Q_{le} through a standard latent-heat conversion.

Dynamic model inputs are assembled as continuous daily gridded drivers. Meteorological forcing is derived from ERA5-Land (Muñoz-Sabater et al., 2021), time-varying LAI from GIMMS (Cao et al., 2023), and atmospheric CO_2 from a daily Mauna Loa record interpolated to the model time axis. For site simulations, the same gridded forcings used in the full-domain simulations are sampled at the flux-site grid cell, with a mean–standard-deviation bias correction toward site observations. This preserves a shared gridded data basis between site training and regional simulations while reducing systematic site-to-grid forcing differences where site observations are available. The uncertainty raised by the remaining site-to-grid mismatch

https://doi.org/10.5194/egusphere-2026-3294
Preprint. Discussion started: 29 July 2026

is discussed in Sect. 5.1. Static environmental attributes are prepared on the same 0.1° grid and provide the inputs to spatially varying parameter mappings. These attributes include hydroclimatic, topographic, groundwater, lithological, and land-cover descriptors rasterized from HydroATLAS fields (Linke et al., 2019), soil properties from SoilGrids aggregated over soil layers (Poggio et al., 2021), and ESA CCI plant functional type fractions (Harper et al., 2023). Raw static variables are retained for diagnosis, and normalized versions are computed using the distribution of valid gridded land pixels over the European domain before being used by the neural-network parameter mappings. For this illustration, the parameter mappings take 11 normalized attributes as input, including forest fraction, groundwater depth, long-term mean potential evapotranspiration, long-term mean precipitation, slope, soil water capacity, long-term mean temperature, sand fraction, bulk density, clay fraction, and soil organic carbon. The same attribute definitions are sampled at flux-site grid cells during training and evaluated across the full European grid for spatial application. The parameter mappings and training objective are described in Sect. 3.2.

3.2 Parameterization experiments

Within the framework's parameter-source declaration (Sect. 2.2), the illustration assembles four parameterization experiments as a nested learning design. All four share the same process equations, forcing data, observational targets, cross-validation splits, and training settings. They differ only in which parameters are learned from environmental attributes and which remain prescribed at their default values (Table 2). Comparing these experiments evaluates whether additional learnable parameter groups improve predictive performance, spatial transferability, and parameter identifiability.

Table 2. Parameterization experiments and learnable parameter assignments.

Experiment	Symbol	Parameter	Unit	Bounds
Baseline (prescribed)	All parameters prescribed at default specification			
Exp. 1 (veg): Vegetation-focused	$g_{\mathrm{s,max}}$	Max. stomatal conductance	$\mathrm{mmol\,m^{-2}\,s^{-1}}$	[100, 800]
	$\psi_{\mathrm{soil,50}}$	Soil water potential at half-max g_{s}	MPa	[−0.5, −0.05]
	ϵ_{L}	Light-use efficiency	$\mathrm{gC\,MJ^{-1}}$	[0.8, 1.5]
Exp. 2 (hydro): Soil- and snow-focused	k_{ss}	Soil surface resistance moisture sensitivity	–	[3.0, 8.0]
	b_{inf}	Infiltration-capacity shape parameter	–	[0.1, 0.8]
	c_{melt}	Degree-day melt coefficient	$\mathrm{mm\,^{\circ}C^{-1}\,d^{-1}}$	[1.0, 8.0]
Exp. 3 (comb): Combined	All parameters from Exp. 1 (veg) and Exp. 2 (hydro)			

All parameters not listed are prescribed at their default specification (Appendix C). All learnable parameters use attribute-based representation. Bounds define the feasible ranges enforced during optimization and combine reported parameter ranges across European vegetation types (e.g., Niu et al., 2011; Lawrence et al., 2019) with practical adjustments.

The baseline serves as the reference without observation-driven parameter learning, with each parameter taking its default specification, which is either a globally uniform value, a plant-functional-type-weighted value, or a value derived from soil texture through pedotransfer functions; these defaults follow conventions in established LSMs with practical adjustments where

https://doi.org/10.5194/egusphere-2026-3294
Preprint. Discussion started: 29 July 2026

needed (Appendix C). Exp. 1 (veg) tests whether learning vegetation controls on canopy conductance, water-stress regulation, and light-use efficiency improves ET and GPP. Exp. 2 (hydro) tests the effect of learning soil evaporation resistance, infiltration partitioning, and snowmelt controls. Exp. 3 (comb) learns all six parameters simultaneously. These parameters illustrate the framework across vegetation, soil, and snow processes; other model parameters can be learned through the same mechanism.

For each learned physical parameter, ADELM uses an independent attribute-to-parameter mapping. Because the model is differentiable end to end, this mapping can be any differentiable function of the static attributes; in the experiments presented here, each mapping is implemented as an MLP with one hidden layer of eight units. The network inputs are the normalized static environmental attributes described in Sect. 3.1, and the output is transformed to remain within the feasible bounds listed in Table 2. Given the limited number of training sites, each mapping uses a deliberately small network to limit overfitting; preliminary tests showed little sensitivity to the number of hidden units within [4, 32] or to the number of hidden layers within [1, 2], and a single hidden layer of 8 units per learned parameter was retained for efficiency and robustness with the available sample size.

Model training minimizes a composite ET and GPP loss across the training sites,

$$\mathcal{L} = \sum_{v \in \{\mathrm{ET},\mathrm{GPP}\}} \alpha_v \left(\mathcal{L}_v^{\mathrm{sample}} + \mathcal{L}_v^{\mathrm{site}} \right), \tag{16}$$

where $\mathcal{L}_v^{\mathrm{sample}} = 1 - \mathrm{NSE}_v^{\mathrm{sample}}$ pools all finite site-day samples and constrains day-to-day and seasonal variability within sites, and $\mathcal{L}_v^{\mathrm{site}} = 1 - \mathrm{NSE}_v^{\mathrm{site}}$ is computed from one multi-year mean flux per site (using sites with at least 365 valid samples, and dropped when fewer than 10 such sites are available) and constrains climatological differences across locations, the signal most relevant to learning attribute-to-parameter mappings that transfer in space. ET and GPP are weighted equally ($\alpha_v = 0.5$); preliminary tests with 2:1 and 1:2 ET:GPP weight ratios did not qualitatively change the experiment ranking. For observed and simulated values, NSE is defined as

$$\mathrm{NSE} = 1 - \frac{\sum_i \left(y_i^{\mathrm{obs}} - y_i^{\mathrm{sim}} \right)^2}{\sum_i \left(y_i^{\mathrm{obs}} - \overline{y}^{\mathrm{obs}} \right)^2}. \tag{17}$$

Gradients of the loss with respect to the learnable network weights are computed by automatic differentiation through the full ADELM forward model. Training and evaluation use random spatial 5-fold cross-validation, with approximately 80% of sites used for parameter learning and 20% held out in each fold. The networks are trained for up to 100 epochs with a learning rate of 0.05, weight decay of 10^{-2}, and gradient clipping at 1.0, with early stopping after 5 epochs without improvement and learning-rate reduction on plateau. The learning rate, weight decay, and gradient clipping were selected by grid search over a representative training subset and retained across all experiments.

3.3 Evaluation

This study evaluates ADELM's performance through held-out site flux skill, gridded spatial behavior, and learned parameter structure. Site-level skill is assessed using the held-out sites from the spatial cross-validation folds. For each experiment, simulated and observed ET and GPP are compared using NSE as defined in Sect. 3.2, computed at two aggregation levels. The

https://doi.org/10.5194/egusphere-2026-3294
Preprint. Discussion started: 29 July 2026

pooled site-day metric evaluates daily flux variability across all held-out samples, and the site-month metric evaluates monthly mean flux dynamics after reducing daily noise.

Spatial behavior is assessed by applying the trained parameterization mappings to the full 0.1° European domain. The gridded simulations are summarized in two ways. First, simulated values are sampled from flux-site grid cells and compared with site observations and gridded reference products. Second, domain-wide fields are aggregated within the biogeographical regions of Europe to examine regional annual means and monthly climatologies. Gridded ET is compared with GLEAM v4 (Miralles et al., 2025) and FLUXCOM X-BASE (Nelson et al., 2024), hereafter FLUXCOM, and gridded GPP with GOSIF (Li and Xiao, 2019) and FLUXCOM.

For experiments with learnable parameters, evaluation also includes the inferred parameter fields. We examine their spatial pattern, variability across cross-validation folds, and relationships with environmental attributes such as mean annual temperature, precipitation, soil texture, and soil organic carbon. For $g_{\mathrm{s,max}}$, inferred values at flux-site grid cells are also compared with flux-derived reference estimates grouped by plant functional type (Liu et al., 2022). These diagnostics assess whether learned parameter fields remain physically coherent and identifiable when different parameter groups are opened to learning.

The choices of attribute set, parameter groups, observational constraints, and cross-validation protocol described here represent one configuration of the framework. Other setups, including different observational data streams (Sect. 2.3) and temporal cross-validation, are supported by the same code base via configuration changes.

4 Results

4.1 Site-level performance

At held-out eddy covariance sites, ADELM reproduces GPP more consistently than ET under the prescribed baseline, and the benefit of observation-constrained parameterization is concentrated in ET (Fig. 5). At the site-daily scale (Fig. 5a), prescribed GPP has a median per-site NSE of 0.51 (interquartile range [0.36, 0.65]), and the learned parameterizations produce similar distributions, with median NSE values of 0.57, 0.51, and 0.52 for Exp. 1 (veg), Exp. 2 (hydro), and Exp. 3 (comb). This weak response suggests that the prescribed model already captures much of the daily GPP variability at these European sites. Prescribed ET has much lower and more variable daily skill, with a median per-site NSE of 0.09 (interquartile range [-0.41, 0.51]) and 28 sites with negative NSE. Learning shifts the ET distribution upward to median NSE values of 0.50, 0.29, and 0.46 for the three experiments, with the largest improvement under the vegetation-focused experiment and no additional gain from combining both parameter groups. The site-daily gain therefore depends more on which process controls are opened to learning than on the total number of learnable parameters.

Site-month comparisons (Fig. 5b,c) test whether the model captures monthly mean flux magnitudes across held-out sites and years. Prescribed GPP already reaches a site-month NSE of 0.63, and the learned experiments change this value only marginally. Prescribed ET has weaker monthly skill (NSE = 0.27), with a mean positive bias of 0.34 $\mathrm{mm\,d^{-1}}$ and an RMSE of 0.88 $\mathrm{mm\,d^{-1}}$. However, learning vegetation-related parameters corrects this most strongly. Exp. 1 (veg) raises ET site-month NSE to 0.65, reduces bias to -0.03 $\mathrm{mm\,d^{-1}}$, and lowers RMSE to 0.61 $\mathrm{mm\,d^{-1}}$. The improvement spans the ET range,

https://doi.org/10.5194/egusphere-2026-3294
Preprint. Discussion started: 29 July 2026

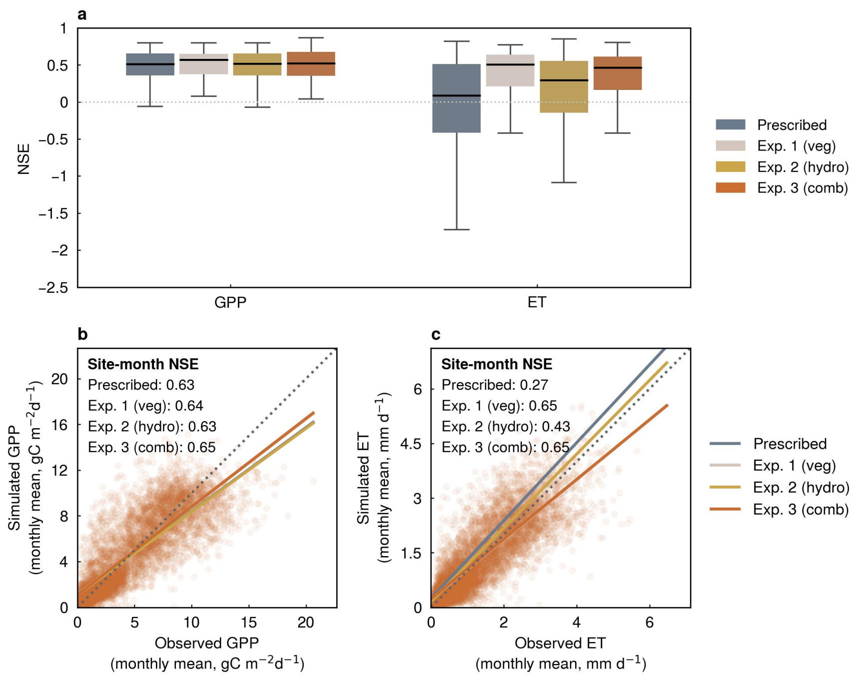

Figure 5. Held-out site-level performance of ADELM across parameterization experiments. (a) Distribution of per-site daily NSE for GPP and ET for the prescribed baseline and three observation-constrained parameterizations. (b–c) Site-month mean simulated versus observed GPP and ET. Points indicate monthly mean site observations and simulations pooled across held-out sites and evaluation years in Exp. 3 (comb), fitted lines summarize each experiment, and the dashed gray line indicates the 1:1 relationship. NSE values in panels (b–c) are computed at the site-month level.

with RMSE falling from 0.45 to 0.35 $\mathrm{mm\,d^{-1}}$ in the low tercile, from 0.95 to 0.61 $\mathrm{mm\,d^{-1}}$ in the middle, and from 1.11 to 0.78 $\mathrm{mm\,d^{-1}}$ in the high. GPP site-month NSE increases only from 0.63 to 0.64, so the vegetation parameters mainly correct water flux while leaving carbon flux largely unchanged.

In contrast, learning soil- and snow-related parameters produces a weaker correction. Exp. 2 (hydro) raises ET site-month NSE from 0.27 to 0.43, reduces mean ET bias from 0.34 to 0.18 $\mathrm{mm\,d^{-1}}$, and lowers RMSE from 0.88 to 0.78 $\mathrm{mm\,d^{-1}}$; the per-site median monthly NSE increases from 0.29 to 0.49. Soil surface resistance, infiltration partitioning, and snowmelt timing therefore affect part of the ET variability but do not correct the dominant overestimation as strongly as the vegetation parameters. GPP site-month NSE remains at 0.63, consistent with the weaker direct connection between these parameters and canopy carbon uptake. The combined experiment matches the vegetation-focused experiment without exceeding it. Exp. 3 (comb) reaches site-month ET NSE of 0.65, bias $-0.02\,\mathrm{mm\,d^{-1}}$, and RMSE of 0.61 $\mathrm{mm\,d^{-1}}$. Adding soil- and snow-parameter flexibility therefore yields no further gain in held-out flux prediction beyond the vegetation-focused setup, though it may still affect the inferred spatial parameter fields (Sect. 4.3).

https://doi.org/10.5194/egusphere-2026-3294
Preprint. Discussion started: 29 July 2026

4.2 Spatial flux patterns

After evaluating ADELM at held-out flux sites, we apply the same learned parameterizations across the European grid to examine the spatial flux fields they produce (Figs. 6a and 7a). We first compare full-domain patterns, regional means, and seasonal cycles with gridded reference products, then use site observations as a site-anchored check at flux-site grid cells, and finally use cross-validation variability to assess sensitivity to the training-site subset.

The full-domain GPP simulation from Exp. 3 (comb) shows a coherent large-scale pattern across Europe, with higher annual GPP in temperate and humid regions and lower values in northern high latitudes, mountain ranges, Mediterranean drylands, and eastern steppic areas (Fig. 6a). Regional annual means indicate moderate differences among ADELM experiments (Fig. 6b). Exp. 1 (veg) and Exp. 3 (comb) generally increase annual GPP relative to the prescribed baseline in Atlantic, Boreal, Continental, and Pannonian Europe, while changes are small in Alpine regions and more mixed in Anatolian, Mediterranean, and Steppic regions. Relative to the gridded reference products, ADELM falls below both GOSIF and FLUXCOM in Atlantic Europe, exceeds both products in Boreal and Continental Europe, and remains closer to the reference range in Alpine, Mediterranean, Pannonian, and Steppic regions. Grid-wise correlations between simulated and reference monthly climatologies are high in Alpine, Atlantic, Boreal, and Continental regions, with median correlations generally above 0.9 for both GOSIF and FLUXCOM (Fig. 6c–d), and lower and more variable in Mediterranean, Pannonian, and Steppic regions. ADELM captures the timing of the growing-season peak in all regions, while differences among experiments are expressed mainly in peak amplitude (Fig. 6e–l). In Atlantic Europe, all ADELM experiments underestimate peak-season GPP relative to GOSIF and FLUXCOM. In Boreal Europe, Exp. 1 (veg) and Exp. 3 (comb) produce higher summer GPP than both reference products. In Continental Europe, all experiments reproduce the seasonal shape closely, with small differences in peak magnitude. In Mediterranean and Steppic regions, the experiments span a broader range of amplitudes, with the prescribed baseline and Exp. 2 (hydro) often giving the highest seasonal peak.

The full-domain ET simulation shows a spatial pattern related to the GPP field but more strongly affected by parameterization (Fig. 7a). Annual ET is highest in humid and energy-available regions and lower in northern, mountainous, and water-limited parts of Europe. Regional annual means show a clearer separation among experiments than for GPP (Fig. 7b). In most regions, the prescribed baseline gives the highest ET, indicating that the default parameterization is generally too wet at the regional scale. Exp. 1 (veg) and Exp. 3 (comb) reduce annual ET across most regions and usually move ADELM closer to GLEAM and FLUXCOM, whereas Exp. 2 (hydro) typically lies between the prescribed baseline and the vegetation-focused experiments. This pattern is especially clear in Atlantic, Boreal, Continental, and Mediterranean Europe, where vegetation-parameter learning substantially reduces ET relative to the baseline. Grid-wise correlations with GLEAM and FLUXCOM are high in Alpine, Atlantic, Boreal, and Continental regions, and lower or more variable in Anatolian, Mediterranean, Pannonian, and Steppic regions (Fig. 7c–d). Differences among experiments are concentrated near the growing-season peak, while winter ET remains similar across experiments (Fig. 7e–l). In most regions, the prescribed baseline produces the highest summer ET, whereas Exp. 1 (veg) and Exp. 3 (comb) reduce the peak and often bring it closer to the reference products. Exp. 2 (hydro) usually gives an intermediate seasonal cycle, consistent with its weaker influence on ET at the site level. In the Pannonian and Steppic

https://doi.org/10.5194/egusphere-2026-3294
Preprint. Discussion started: 29 July 2026

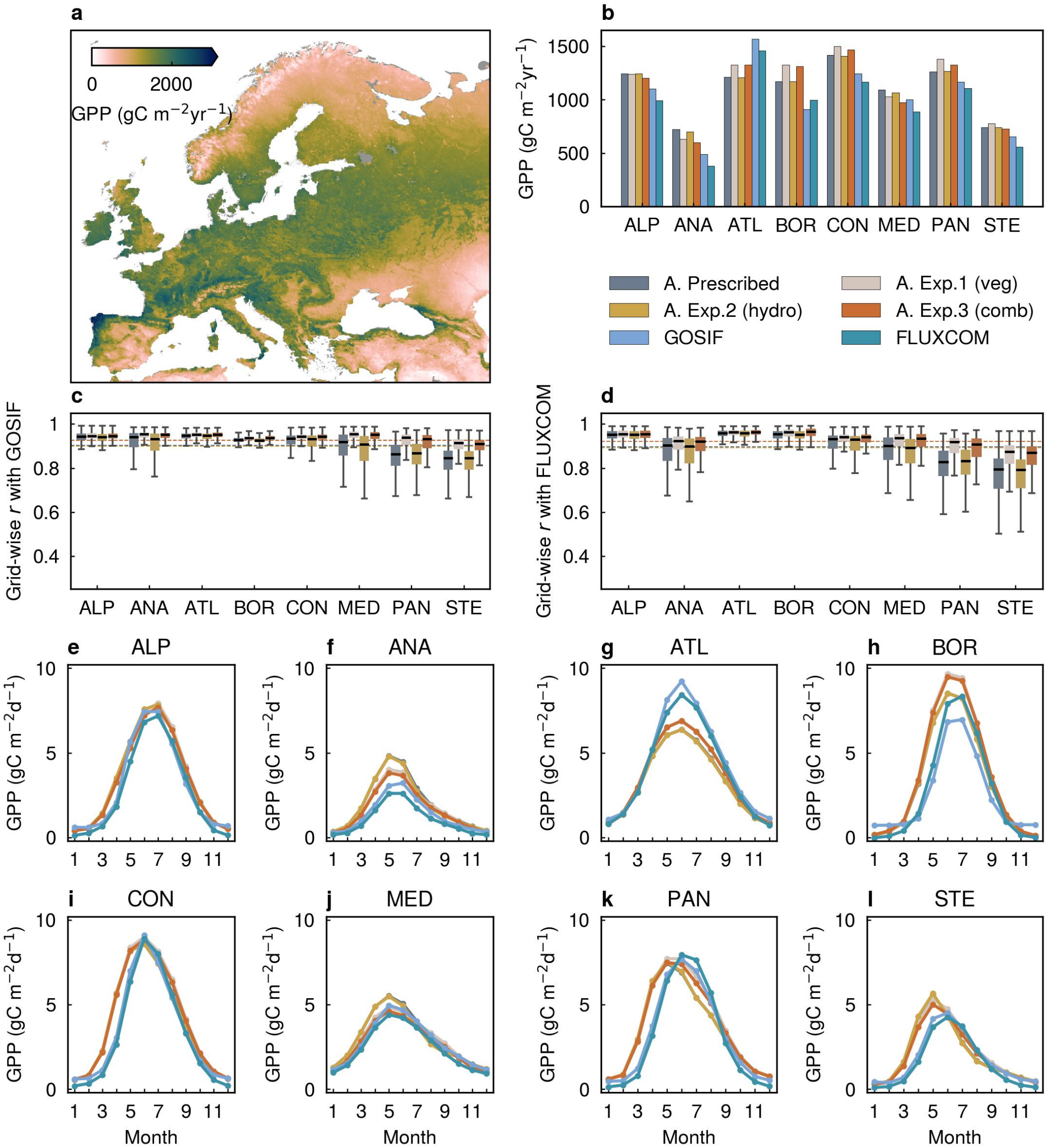

Figure 6. Full-domain spatial evaluation of simulated gross primary productivity (GPP) across Europe. (a) Annual GPP from ADELM Exp. 3 (comb). (b) Regional annual GPP for the prescribed baseline, Exp. 1 (veg), Exp. 2 (hydro), and Exp. 3 (comb), compared with GOSIF and FLUXCOM across the eight biogeographic regions. (c–d) Distribution of grid-wise Pearson correlation coefficients between simulated and reference monthly GPP climatologies, shown by region for GOSIF (c) and FLUXCOM (d). The dashed orange line indicates the pan-European mean correlation across experiments and reference products. (e–l) Regional mean monthly GPP climatology for each biogeographic region: ALP = Alpine, ANA = Anatolian, ATL = Atlantic, BOR = Boreal, CON = Continental, MED = Mediterranean, PAN = Pannonian, STE = Steppic.

https://doi.org/10.5194/egusphere-2026-3294
Preprint. Discussion started: 29 July 2026

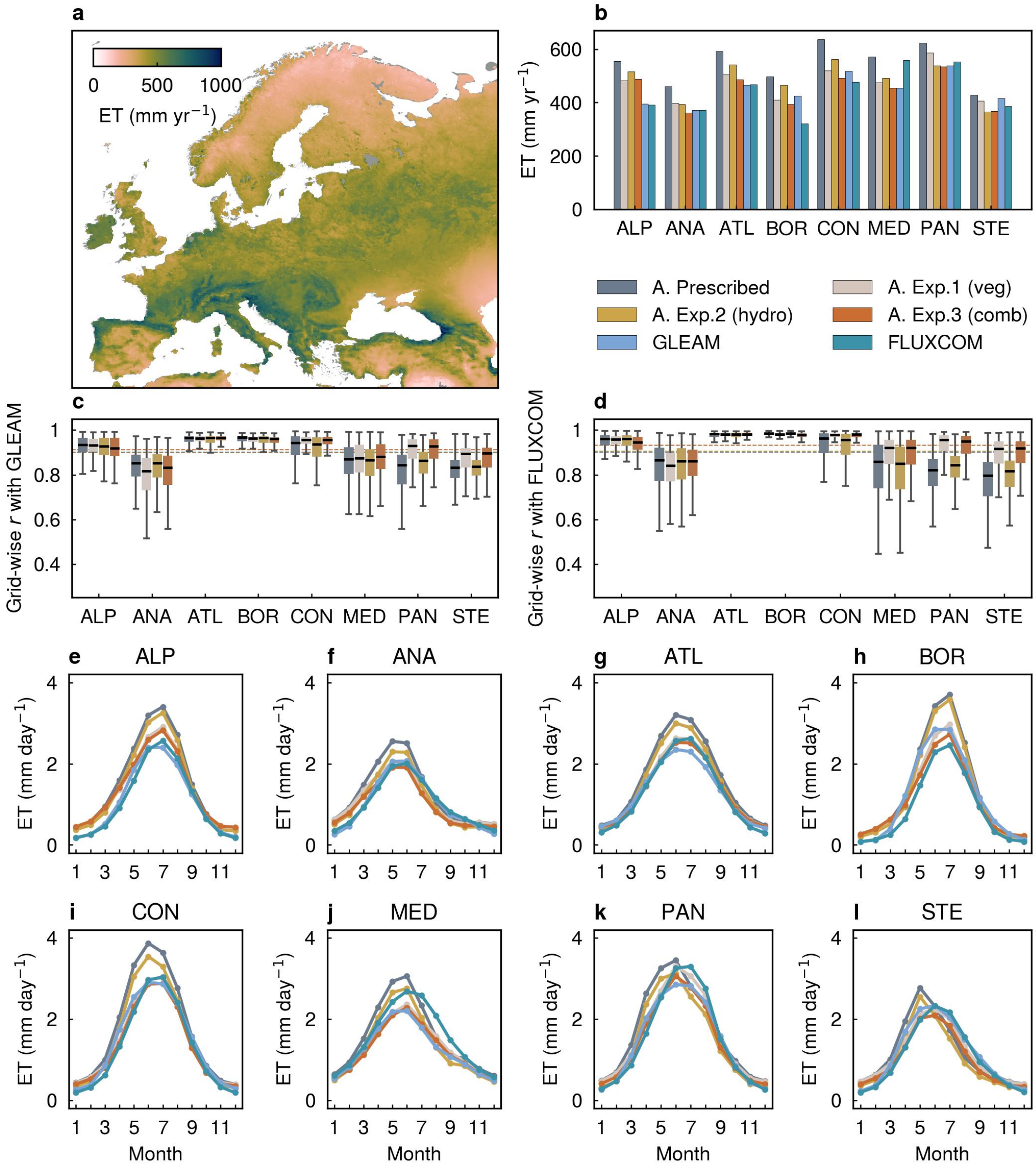

Figure 7. Full-domain spatial evaluation of simulated evapotranspiration (ET) across Europe. (a) Annual ET from ADELM Exp. 3 (comb). (b) Regional annual ET for the prescribed baseline, Exp. 1 (veg), Exp. 2 (hydro), and Exp. 3 (comb), compared with GLEAM and FLUXCOM across the eight biogeographic regions. (c–d) Distribution of grid-wise Pearson correlation coefficients between simulated and reference monthly ET climatologies, shown by region for GLEAM (c) and FLUXCOM (d). The dashed orange line indicates the pan-European mean correlation across experiments and reference products. (e–l) Regional mean monthly ET climatology for each biogeographic region. Region abbreviations follow Fig. 6.

https://doi.org/10.5194/egusphere-2026-3294
Preprint. Discussion started: 29 July 2026

regions, Exp. 1 (veg) and Exp. 3 (comb) are closer to the reference seasonal cycles than the prescribed baseline and Exp. 2 (hydro), especially near the summer peak and late-season decline.

Sampling ADELM Exp. 3 (comb) and the reference products at flux-site grid cells provides a site-anchored check (Fig. 8). For GPP, ADELM preserves the observed cross-site gradient in site means, with an R^2 of 0.48, similar to GOSIF and FLUXCOM (R^2 =0.42 and 0.46; Fig. 8a). ADELM also captures the observed seasonal timing in the Alpine, Atlantic, Boreal, Continental, and Mediterranean regions (Fig. 8b–g), with peak-season GPP slightly low in the Alpine region, close to observations in Atlantic and Continental regions, and somewhat high in the Boreal region. The Pannonian comparison is based on one site only, and all gridded estimates miss its large observed summer peak. For ET, ADELM Exp. 3 (comb) also preserves the observed cross-site gradient, with an R^2 of 0.46, while the corresponding relationships are weaker for GLEAM ($R^2 = 0.05$) and FLUXCOM ($R^2 = 0.26$; Fig. 8h). Despite the different spatial supports of tower footprints, ADELM grid cells, and reference pixels, ADELM retains more of the site-observed cross-site ET contrast at these locations. ADELM reproduces the ET seasonal timing in most regions with differences mainly in amplitude (Fig. 8i–n), close to the observed summer peak in several regions, slightly high in the Alpine region, and lower than the single Pannonian site near the summer maximum.

The five cross-validation folds provide a final check on how strongly the gridded flux fields depend on the subset of sites used for training (Fig. 9). For GPP, fold-to-fold variability is generally low across most of Europe. Exp. 2 (hydro) shows the weakest variability, consistent with its small effect on GPP in both the site-level and gridded evaluations. Exp. 1 (veg) and Exp. 3 (comb) produce higher GPP coefficient of variation (CoV) in mountainous and southern European regions, especially around the Alps, the Balkans, and parts of the Mediterranean domain. For ET, fold sensitivity is larger and more spatially extensive. Exp. 1 (veg) increases CoV in parts of northern Europe, mountainous regions, and southern Europe, while Exp. 3 (comb) produces the broadest high-CoV pattern, with elevated variability across Scandinavia, eastern Europe, mountain belts, and water-limited southern regions. Exp. 2 (hydro) remains comparatively stable, but also gives smaller ET improvements. The parameter groups that most improve ET therefore make the gridded ET field more sensitive to which sites are used for training.

4.3 Learned parameter structure

We next examine whether the learned attribute-to-parameter mappings produce physically coherent and identifiable parameter fields beyond improved flux predictions. We focus on maximum stomatal conductance, $g_{\mathrm{s,max}}$, which is learned in both Exp. 1 (veg) and Exp. 3 (comb) and has external references for independent comparison. By scaling the stomatal opening through which leaves both lose water and take up CO_2, it regulates both ET and GPP.

The inferred $g_{\mathrm{s,max}}$ fields show coherent spatial structure in both Exp. 1 (veg) and Exp. 3 (comb) (Fig. 10a, c). Higher values occur mainly in northern, humid, and temperate parts of the domain, while lower values occur in southern Europe and other drier regions. The mapping generates this pattern directly from environmental attributes, without plant-functional-type categorization. The two experiments differ more clearly in stability than in broad spatial pattern. Exp. 1 (veg) produces a smoother field with relatively low fold-to-fold variability, whereas Exp. 3 (comb) shows much higher coefficient of variation across large parts of the domain, especially in northern Europe, mountain belts, and water-limited southern regions (Fig. 10b, d). Adding soil and snow parameters therefore increases fold-to-fold variability in the inferred $g_{\mathrm{s,max}}$ field.

https://doi.org/10.5194/egusphere-2026-3294
Preprint. Discussion started: 29 July 2026

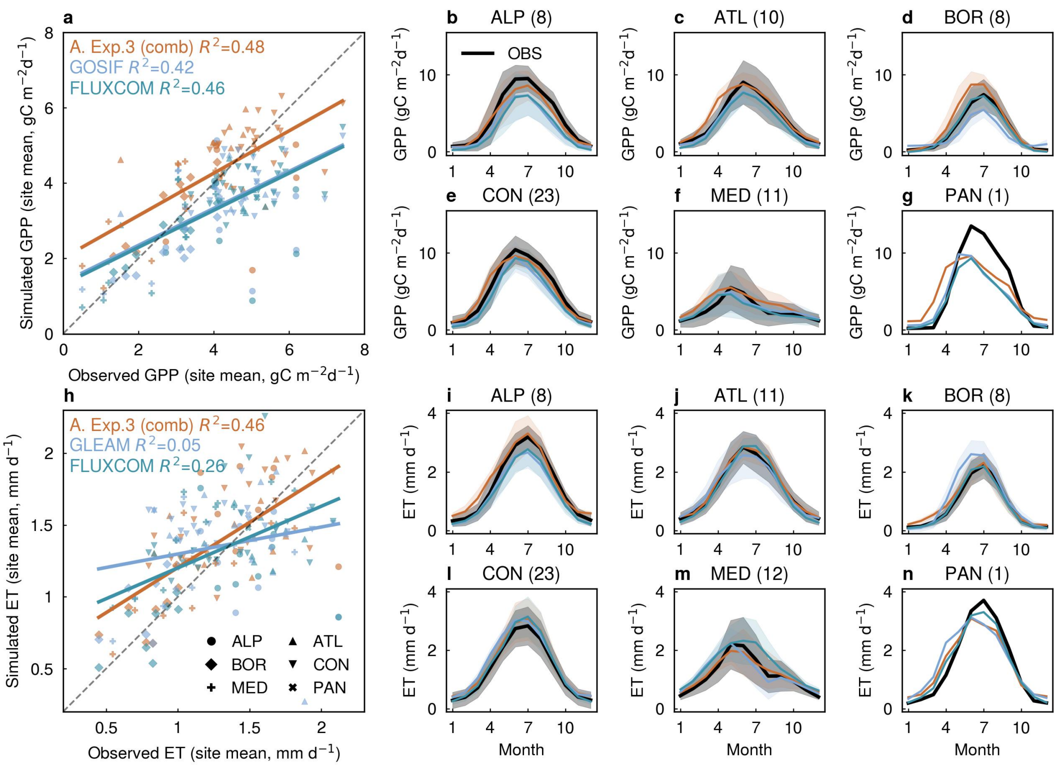

Figure 8. Site-anchored evaluation of ADELM Exp. 3 (comb) at flux-site grid cells. ADELM and reference-product values are sampled at the grid cells or pixels containing eddy covariance towers and averaged over the matched evaluation period before comparison with site observations. (a, h) Site-mean simulated versus observed GPP and ET, compared with GOSIF for GPP, GLEAM for ET, and FLUXCOM for both variables. Points are grouped by biogeographical region, and fitted lines summarize the cross-site climatological gradient for each product. (b–g, i–n) Regional monthly climatologies of observed and simulated GPP and ET at flux-site grid cells. Shaded ranges indicate variability among sites within each region. Numbers in parentheses indicate the number of sites.

The reference values from Liu et al. (2022), which represent ecosystem-scale unstressed stomatal conductance inferred from FLUXNET observations, give an external check on the learned $g_{\mathrm{s,max}}$ field (Fig. 10e, f). Exp. 1 (veg) produces $g_{\mathrm{s,max}}$ values broadly comparable to this benchmark in both magnitude and plant functional type ordering, with grassland sites occupying the higher-$g_{\mathrm{s,max}}$ part of the distribution and group means following the reference ordering relatively well. Exp. 3 (comb) shows a weaker relationship, with larger scatter and less distinct separation among plant functional types. Learning vegetation parameters alone therefore yields a more identifiable $g_{\mathrm{s,max}}$ field, whereas the additional soil and snow parameters in Exp. 3 (comb) allow part of the flux constraint to be absorbed by other process controls.

Relationships with environmental attributes show how the learned mappings organize $g_{\mathrm{s,max}}$ variation (Fig. 10g–n). In Exp. 1 (veg), inferred $g_{\mathrm{s,max}}$ decreases with mean annual temperature and clay fraction, and increases with mean annual precipitation and soil organic carbon, consistent with higher conductance in wetter and more productive environments. In Exp. 3 (comb),

https://doi.org/10.5194/egusphere-2026-3294
Preprint. Discussion started: 29 July 2026

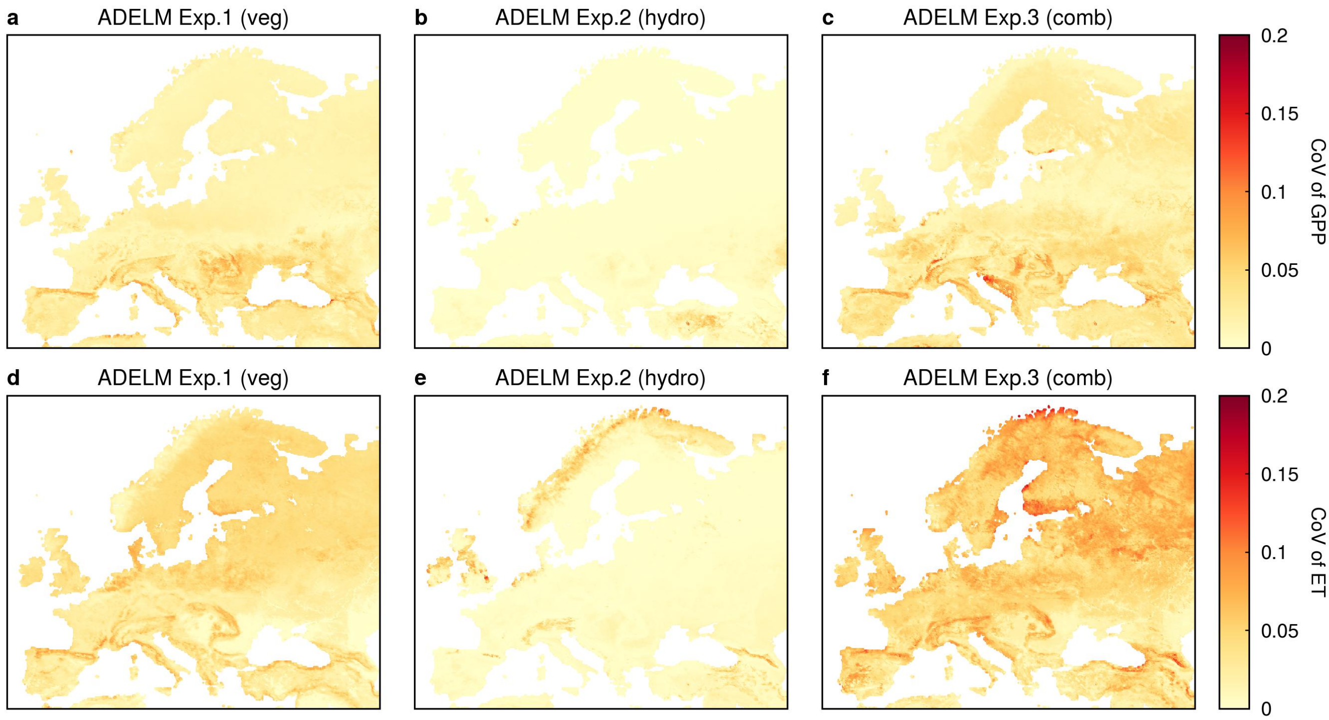

Figure 9. Cross-validation variability of gridded flux simulations. Panels show the coefficient of variation (CoV) across the five fold-trained parameterization mappings after each mapping is evaluated over the full European domain. (a–c) CoV of annual GPP for Exp. 1 (veg), Exp. 2 (hydro), and Exp. 3 (comb). (d–f) CoV of annual ET for Exp. 1 (veg), Exp. 2 (hydro), and Exp. 3 (comb). Higher values indicate grid cells where the simulated flux is more sensitive to the subset of flux sites used to train the parameter mapping.

these relationships weaken for mean annual temperature, precipitation, and clay fraction, while the positive relationship with soil organic carbon remains visible. The weakening suggests that opening soil and snow parameters allows the optimization to redistribute flux corrections among multiple process controls.

Similar held-out flux skill can therefore correspond to different parameter structures. Exp. 1 (veg) and Exp. 3 (comb) produce comparable GPP and ET performance, but Exp. 1 (veg) gives a more stable conductance field, clearer environmental relationships, and closer agreement with the external conductance benchmark. Increasing the number of learnable parameters can introduce compensation among process controls, limiting the identifiability of individual parameter fields even when predictive skill remains comparable. We discuss this further in Sect. 5.1.

https://doi.org/10.5194/egusphere-2026-3294
Preprint. Discussion started: 29 July 2026

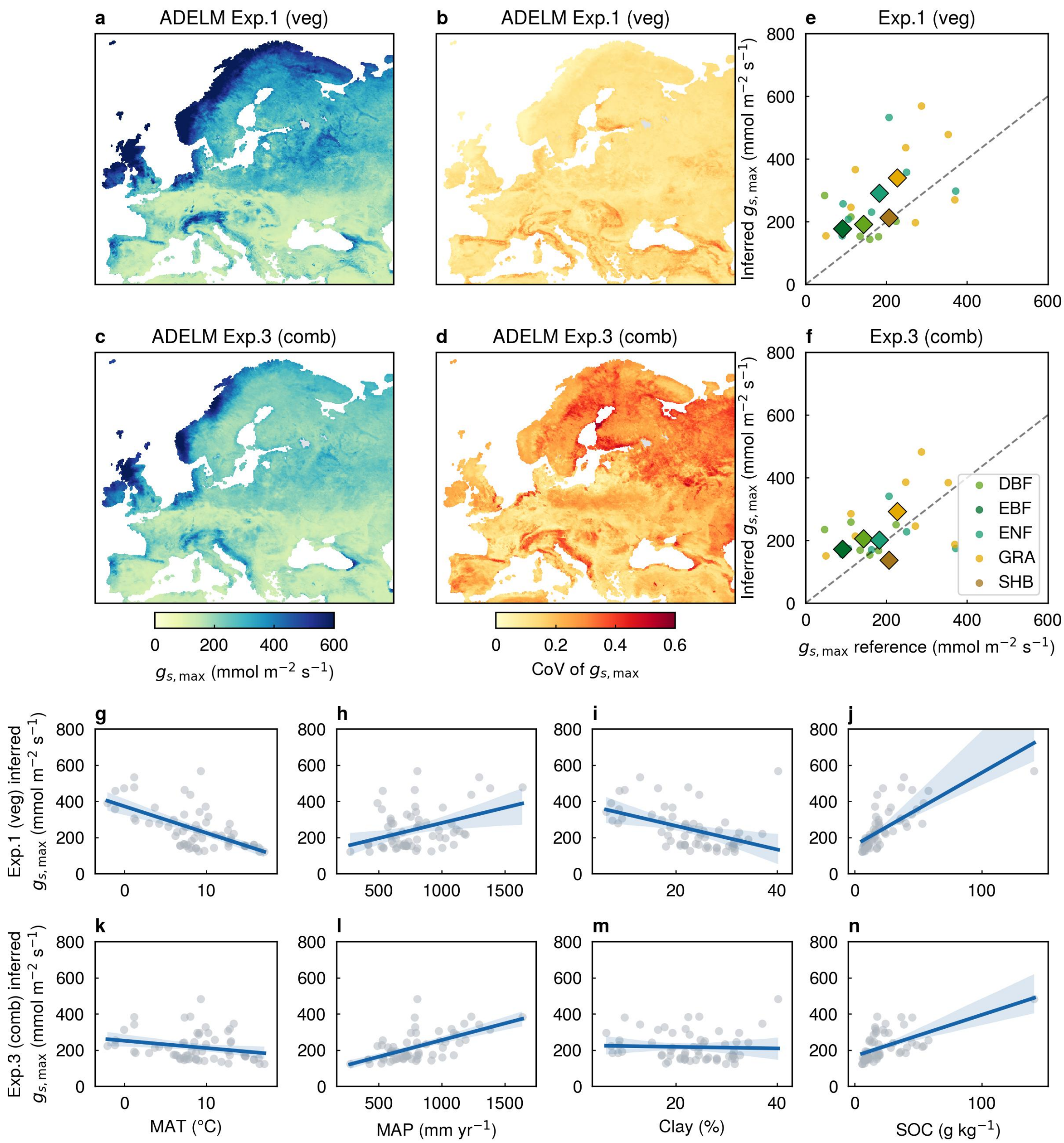

Figure 10. Learned structure and stability of maximum stomatal conductance $g_{\mathrm{s,max}}$. (a, c) Inferred $g_{\mathrm{s,max}}$ fields for Exp. 1 (veg) and Exp. 3 (comb) evaluated over the European grid. (b, d) Coefficient of variation of inferred $g_{\mathrm{s,max}}$ across the five fold-trained mappings. (e, f) Comparison between ADELM-inferred $g_{\mathrm{s,max}}$ and the flux-derived reference values of Liu et al. (2022) at flux-site grid cells, grouped by plant functional type. Small points indicate individual sites and diamonds indicate group means. (g–j) Relationships between Exp. 1 (veg) inferred $g_{\mathrm{s,max}}$ and mean annual temperature (MAT), mean annual precipitation (MAP), clay fraction, and soil organic carbon (SOC) at flux-site grid cells. (k–n) Corresponding relationships for Exp. 3 (comb). Blue lines and shaded bands indicate fitted trends and associated uncertainty.

https://doi.org/10.5194/egusphere-2026-3294
Preprint. Discussion started: 29 July 2026

5 Discussion

5.1 Parameter learning and identifiability

Hybrid frameworks that combine machine learning with process-based models are typically motivated by complementary strengths. Machine learning provides flexibility where process structure is uncertain, while the process structure regularizes the learned components where observations are sparse. The expectation is that learned parameter fields, anchored to identifiable process parameters with physical meaning, will remain interpretable and transferable to new conditions. Equifinality is a long-standing concern in process-based modeling, where different parameter sets can produce nearly the same flux response when the observational constraint is weaker than the parametric flexibility (Beven, 2006). The added flexibility of a machine-learned attribute-to-parameter mapping may even worsen the situation (Fang and Gentine, 2024; ElGhawi et al., 2023; Baghirov et al., 2025). The mapping itself can take many functional forms that all fit the fluxes equally well, and these flexible mappings can absorb process-model structural errors at the parameter level, because the model exploits attribute-output correlations without resolving the underlying mechanism (Jiang et al., 2024).

In the present illustration, the learned mappings are constrained by only two integrated fluxes, ET and GPP, at 63 European flux sites used for spatial cross-validation. These fluxes constrain the integrated carbon and water response without separating canopy conductance, soil water supply, snowmelt timing, and energy partitioning. Whether opening additional parameter groups to learning under this constraint helps or hurts the identifiability of individual parameter fields is therefore an empirical question that depends on the specific configuration.

ADELM's parameter-source declaration (Sect. 2.2) makes this kind of test directly possible. By holding the forward model fixed and varying only which parameters are learned, the framework allows side-by-side comparison of parameter-learning configurations and direct inspection of the resulting parameter fields. The contrast between Exp. 1 (veg) and Exp. 3 (comb) shows what such a comparison reveals (Sect. 4.3). With similar held-out flux skill, Exp. 3 (comb) produces a less stable $g_{\mathrm{s,max}}$ field and weaker agreement with the flux-derived benchmark than Exp. 1 (veg) (Figs. 10, 5). In Exp. 3 (comb), each additional learnable parameter opens an alternative pathway for the optimizer to lower the loss, leaving each individual parameter less constrained than in Exp. 1 (veg). The model's effective degrees of freedom expand faster than two integrated fluxes can resolve them.

5.2 Multi-source and multi-scale observational constraints

The data constraint in the present illustration is concentrated at flux-site locations. The 63 European flux sites occupy only part of the continental attribute space, clustered within a narrow region of the gridded attribute cloud (Fig. 11a–h), and parameter estimates outside this region are only loosely tied to flux observations, consistent with the higher cross-validation variability seen in some mountainous, northern, and water-limited regions. Within the trained domain, the six learned parameters separate into qualitatively different patterns (Fig. 11i–n). $g_{\mathrm{s,max}}$, ϵ_{L}, and k_{ss} retain broad spatial distributions across the European grid, while $\psi_{\mathrm{soil,50}}$, b_{inf}, and c_{melt} collapse to near-constant values, indicating that their attribute-to-parameter mappings have not acquired substantive spatial dependence from the flux observations and have effectively reduced to shared formulations.

https://doi.org/10.5194/egusphere-2026-3294
Preprint. Discussion started: 29 July 2026

These near-constant distributions can arise from two distinct sources. For c_{melt}, the realistic range of degree-day melt rates in European snow conditions is itself narrow relative to the prior bounds, and a tightly concentrated learned value is possibly plausible. For $\psi_{\mathrm{soil},50}$ and b_{inf}, however, the collapse more likely reflects that GPP and ET do not carry information sufficient to recover this variation.

These patterns of differential identifiability mainly follow from constraining ADELM with two integrated fluxes alone. GPP and ET are integrated outputs of the full process chain; they constrain net canopy and water exchange but cannot resolve which sub-process generates each component of the response, leaving parameters with overlapping pathways weakly distinguished. Because ADELM is differentiable, any observation that can be aggregated to a simulated state or flux can enter the training objective, and the most useful additions are those that resolve the limitations identified above. Surface or root-zone soil moisture from missions such as SMAP and SMOS (Entekhabi et al., 2010; Kerr et al., 2010) would help separate soil water supply from stomatal regulation, the compensation most visible in the $g_{\mathrm{s,max}}$ fields. Extending ADELM's process representation would open additional observations to assimilation. For example, remote sensed land surface temperature (Fisher et al., 2020) would inform energy partitioning between sensible and latent heat, distinguishing water stress from differences in surface resistance or aerodynamic exchange. Vegetation optical depth could similarly constrain canopy water status (Felton et al., 2025), providing information not captured by the prescribed leaf area index. Moreover, adding leaf or stem water potential as state variables would allow assimilation of microwave-based vegetation water potential estimates (Konings et al., 2021; Anderegg et al., 2018; Holtzman et al., 2021), directly constraining plant hydraulic parameters that flux-only training cannot resolve.

Site fluxes are also limited in scale. Eddy covariance towers measure turbulent fluxes over sub-kilometre footprints, while ADELM parameters and fluxes live on the 0.1° grid. The forcing correction (Sect. 3.1) removes systematic meteorological differences, but vegetation, soil, disturbance, and sub-grid heterogeneity differences remain, and the learned parameters likely absorb these aggregation effects. Adding scale-integrated observations from catchments or satellite pixels constrains the water balance independently of site fluxes and reduces the parameter ambiguity that comes from observing the system at only one scale. For example, catchment streamflow can be compared with ADELM after aggregating grid-cell runoff to basin polygons. Blougouras et al. (2025) recently showed that combining streamflow with ET, snow water equivalent, and terrestrial water storage anomalies stabilizes parameter learning and improves water-balance consistency in a related differentiable ecohydrological framework, an approach directly transferable to ADELM through aggregation to catchments, satellite pixels, or flux-footprint regions. A later implementation could add differentiable routing, so that downstream discharge constrains upstream grid-cell parameters through the channel network (Wang et al., 2024). These constraints would also make the scale dependence of the learned parameters directly testable. For instance, running ADELM at multiple spatial resolutions and comparing the resulting parameter fields with pedotransfer- or trait-based estimates would show whether grid-scale parameters diverge from local relationships in an attribute-dependent way (Van Looy et al., 2017; Anderegg et al., 2022; Paschalis et al., 2022).

5.3 Implications for land model development

Beyond observational under-constraint, the identifiability of learned parameters also depends on the fidelity of the underlying process representation. Where the process structure is simplified, learned parameters can absorb the resulting structural error.

https://doi.org/10.5194/egusphere-2026-3294
Preprint. Discussion started: 29 July 2026

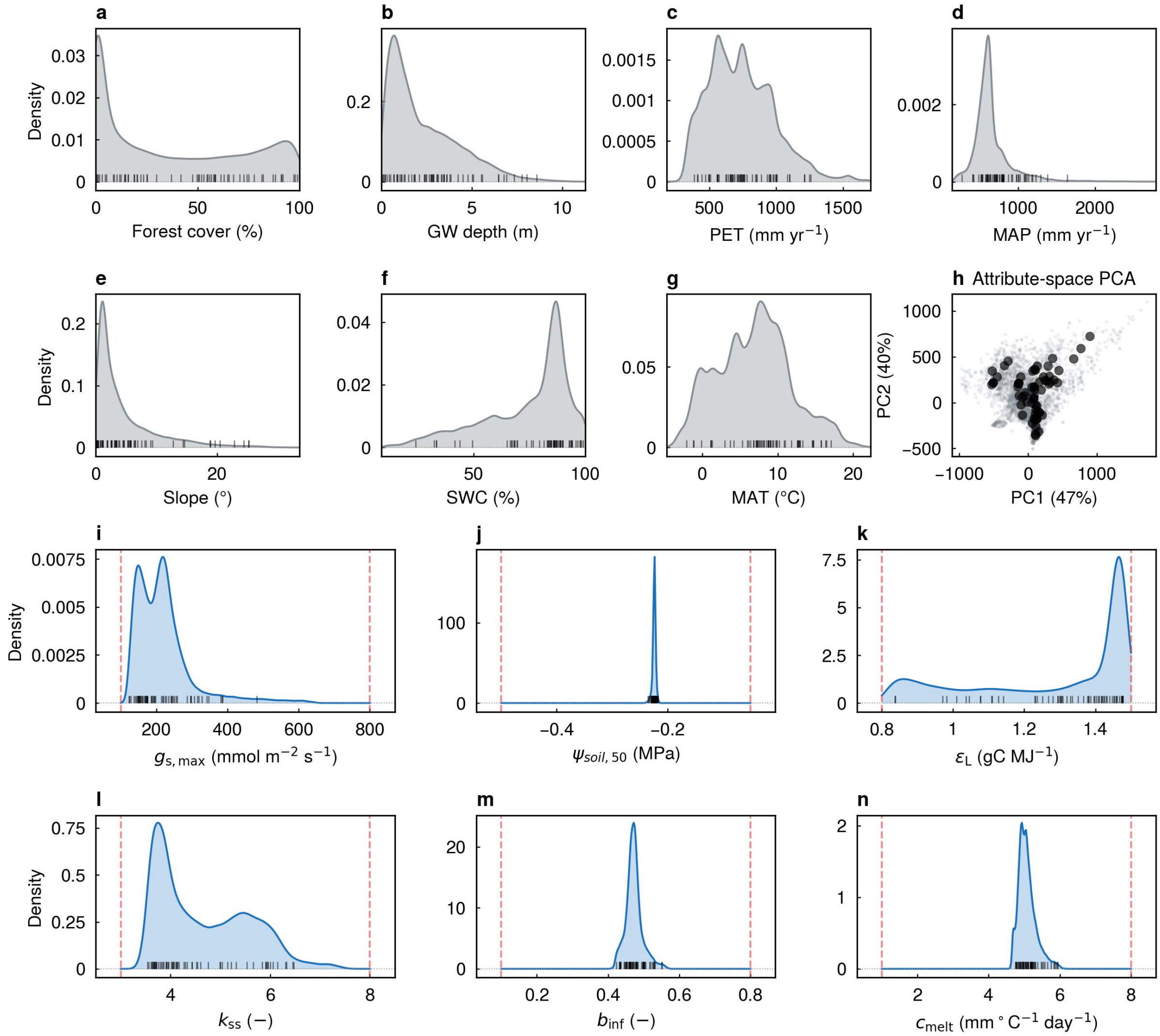

Figure 11. Attribute-space coverage and learned parameter distributions. (a–g) Domain-wide distributions of selected environmental attributes used by the learned parameter mappings, with rug marks indicating flux-site values. Attributes include forest cover, groundwater (GW) depth, potential evapotranspiration (PET), mean annual precipitation (MAP), slope, soil water capacity (SWC), and mean annual temperature (MAT). (h) Principal component analysis (PCA) of the normalized environmental attributes, showing gridded cells in gray and flux sites in black. Percentages indicate the variance explained by each principal component. (i–n) Spatial distributions of the six learned Exp. 3 (comb) parameters across the European grid. Dashed red lines indicate the feasible parameter bounds used during training (Table 2). Rug marks indicate parameter values at flux-site grid cells.

https://doi.org/10.5194/egusphere-2026-3294
Preprint. Discussion started: 29 July 2026

For example, ADELM v1.0 collapses soil–plant hydraulic transport into a single root-weighted soil water potential, with no explicit representation of stem or leaf water potential, hydraulic conductances, or capacitance. Under this representation, hydraulic complexity that would otherwise be carried by additional state variables can be absorbed by the empirical parameters $\psi_{\mathrm{soil},50}$ and $g_{\mathrm{s,max}}$, contributing to the compensation observed in Exp. 3 (comb). Extending ADELM to an explicit soil–plant hydraulics scheme (Torres-Ruiz et al., 2023; Verhoef et al., 2026) would give these parameters a stronger mechanistic anchor.

The same end-to-end differentiability that supports parameter learning in ADELM v1.0 also enables learning process functions. Replacing selected empirical functions with neural functions while keeping them inside the process graph requires gradients to flow through both the learned function and the surrounding physics, which is precisely what automatic differentiation through the coupled ADELM forward model provides (Shen et al., 2023). Related differentiable hybrid work has applied this strategy to inferring stomatal and aerodynamic resistances within a Penman–Monteith constraint (ElGhawi et al., 2023), to global terrestrial evaporation (Koppa et al., 2022), and to hydrological partitioning under water-balance constraints (Kraft et al., 2022). In ADELM, the current Jarvis formulation represents stomatal regulation through separable responses to ambient environmental factors, while these controls interact in reality with atmospheric CO_2, plant hydraulic status, vegetation state, and antecedent stress. A learned conductance function could represent these interactions while remaining embedded in the differentiable land model, with its behavior constrained jointly by ET, GPP, soil moisture, land surface temperature, and other observations through the same differentiable graph. For example, ElGhawi et al. (2025) trained neural parameterizations of coupled photosynthesis and transpiration in JSBACH, embedding learned g_{s}, V_{cmax}, and $J_{\max}$ representations dynamically within the ESM land component. ADELM provides a similar differentiable substrate for testing, diagnosing, and scaling such process formulations across coupled water, energy, and carbon processes.

6 Conclusions

This study introduces ADELM v1.0, a differentiable LSM in which the assignment of each parameter is a configurable design choice within the framework. Process equations, parameter mappings, prognostic updates, and loss share a single automatic-differentiation graph, so observations constrain selected parameters through the same pathways that generate the model outputs. Each parameter can be held prescribed, learned as a globally shared quantity, or learned as a spatial function of environmental attributes. The European case study shows that this design works in practice. Attribute-to-parameter mappings constrained at 63 flux sites transfer to the full 0.1° grid, producing spatially continuous parameter and flux fields, with the clearest improvements in ET where vegetation controls on canopy conductance are learned. Holding the process core fixed also let us compare parameterization choices directly. Across the learning configurations, predictive skill was comparable while parameter structures differed, with the combined experiment producing a less identifiable conductance field than the vegetation-focused one. This kind of contrast, normally hidden when only flux skill is reported, is what ADELM's framework brings into view, supporting more deliberate choices about which parameters to expose to learning.

More broadly, as a differentiable LSM, ADELM v1.0 offers a way to revisit how land models assign their parameters, which still rely largely on prescribed mappings, plant-functional-type tables for vegetation and pedotransfer functions for soil.

https://doi.org/10.5194/egusphere-2026-3294
Preprint. Discussion started: 29 July 2026

Learning these mappings end-to-end from observations identifies which parameters carry environmental dependence that a prescribed mapping does not capture, and such learned parameterizations could in principle replace the prescribed mappings in standard LSMs. This could open the way to achieving parameterizations that can be transferred across diverse climates and ecosystems, and which can be tested systematically.

Code and data availability. The ADELM v1.0 source code used in this study is archived on Zenodo at https://doi.org/10.5281/zenodo.20574230 (Jiang, 2026) and is released under the European Union Public License v. 1.2 (EUPL-1.2). Model documentation, including installation instructions, configuration files, and example workflows, is available at https://adelm.org/ (last access: 12 June 2026).

All input and evaluation data are publicly available from their original data providers. ERA5-Land meteorological forcing is available from the Copernicus Climate Data Store (Muñoz-Sabater et al., 2021). Eddy covariance observations used for training and site evaluation were derived from PLUMBER2, the ICOS Warm Winter 2020 collection, and the ICOS Drought-2018 collection (Ukkola et al., 2022; Warm Winter 2020 Team and ICOS Ecosystem Thematic Centre, 2020; Drought 2018 Team and ICOS Ecosystem Thematic Centre, 2020); flux processing used FluxnetLSM (Ukkola et al., 2017). GIMMS LAI data are available from the GIMMS LAI archive (Cao et al., 2023). Atmospheric CO_2 data are available from the NOAA Global Monitoring Laboratory Mauna Loa record (https://gml.noaa.gov/ccgg/trends/data.html). Static environmental attributes are available from HydroATLAS/BasinATLAS via HydroSHEDS (Linke et al., 2019), ISRIC SoilGrids (Poggio et al., 2021), and ESA CCI land-cover data (Harper et al., 2023). Gridded evaluation products are available from their original providers, including GLEAM v4 (Miralles et al., 2025), FLUXCOM X-BASE (Nelson et al., 2024), and GOSIF (Li and Xiao, 2019).

Appendix A: Supplementary process formulations

A1 Radiative transfer module $\mathcal{M}_{\mathrm{rad}}$

This appendix details the shortwave and longwave components $R^{\mathrm{n}}_{\mathrm{sw,v}}$, $R^{\mathrm{n}}_{\mathrm{sw,g}}$, $R^{\mathrm{n}}_{\mathrm{lw,v}}$, and $R^{\mathrm{n}}_{\mathrm{lw,g}}$ that combine into the net radiation in Eq. (3). The shortwave treatment follows a two-stream canopy scheme (Sellers, 1985; Dickinson, 1983), and the longwave treatment is a broadband thermal exchange among atmosphere, canopy, and ground. The fluxes are summarized schematically in Fig. A1.

Incoming shortwave radiation $R^{\downarrow}_{\mathrm{sw}}$ is partitioned into a visible band (VIS, 400–700 nm) and a near-infrared band (NIR), denoted by $\Lambda \in \{\mathrm{vis}, \mathrm{nir}\}$. Within each band, the downward flux is split into direct-beam and diffuse components,

$$R^{\mu}_{\mathrm{sw},\Lambda} = f_{\Lambda}\, f_{\mathrm{dir}}\, R^{\downarrow}_{\mathrm{sw}}, \tag{A1}$$

$$R^{\mathrm{d}}_{\mathrm{sw},\Lambda} = f_{\Lambda}\,(1 - f_{\mathrm{dir}})\, R^{\downarrow}_{\mathrm{sw}}, \tag{A2}$$

where f_{vis} is the prescribed visible fraction, $f_{\mathrm{nir}} = 1 - f_{\mathrm{vis}}$, and f_{dir} is the fraction of incoming shortwave radiation treated as direct beam.

The ground absorbs the in-band downward shortwave that reaches it and is not reflected by the surface,

$$R^{\mathrm{n}}_{\mathrm{sw,g},\Lambda} = (1 - \alpha_{\mathrm{g},\Lambda}) \left[R^{\mu}_{\mathrm{sw},\Lambda} f_{\mathrm{tdd},\Lambda} + R^{\mu}_{\mathrm{sw},\Lambda} f_{\mathrm{tid},\Lambda} + R^{\mathrm{d}}_{\mathrm{sw},\Lambda} f_{\mathrm{tii},\Lambda} \right], \tag{A3}$$

https://doi.org/10.5194/egusphere-2026-3294
Preprint. Discussion started: 29 July 2026

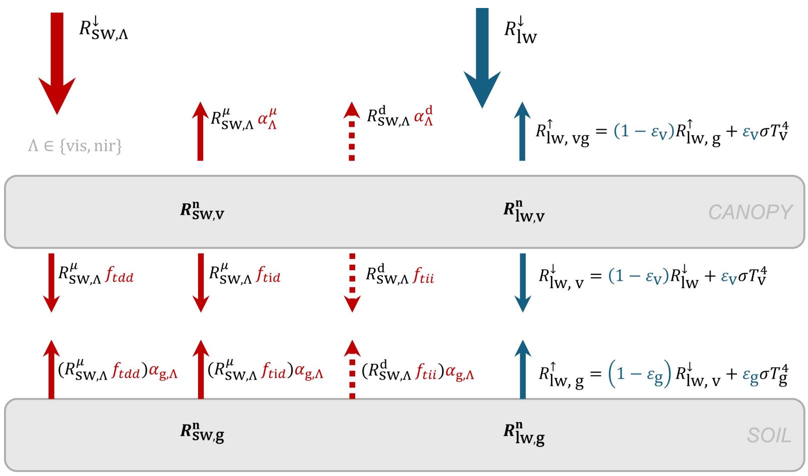

Figure A1. Schematic of the radiative-transfer fluxes used in ADELM v1.0. Red arrows denote shortwave radiation in spectral band $\Lambda \in \{\mathrm{vis}, \mathrm{nir}\}$, and blue arrows denote broadband longwave radiation. Incoming shortwave radiation in each band satisfies $R^{\downarrow}_{\mathrm{sw},\Lambda} = R^{\mu}_{\mathrm{sw},\Lambda} + R^{\mathrm{d}}_{\mathrm{sw},\Lambda}$, where superscripts μ and d denote direct-beam and diffuse components, respectively. The canopy shortwave solution is summarized by direct-beam and diffuse reflectance coefficients, α^{μ}_{Λ} and $\alpha^{\mathrm{d}}_{\Lambda}$, and transmittance coefficients, $f_{\mathrm{tdd},\Lambda}$, $f_{\mathrm{tid},\Lambda}$, and $f_{\mathrm{tii},\Lambda}$. Transmitted shortwave radiation reaches the ground surface, where the band-specific ground albedo $\alpha_{\mathrm{g},\Lambda}$ determines reflected and absorbed fractions. Longwave radiation is exchanged between the atmosphere, canopy, and ground through thermal emission and reflection, with emissivities ε_{v} and ε_{g}.

where $\alpha_{\mathrm{g},\Lambda}$ is the band-specific ground albedo and $f_{\mathrm{tdd},\Lambda}$, $f_{\mathrm{tid},\Lambda}$, $f_{\mathrm{tii},\Lambda}$ are transmittance coefficients. The coefficient $f_{\mathrm{tdd},\Lambda}$ gives the fraction of incident direct-beam radiation transmitted through the canopy as direct beam, $f_{\mathrm{tid},\Lambda}$ gives the fraction of incident direct-beam radiation scattered into downward diffuse radiation, and $f_{\mathrm{tii},\Lambda}$ gives the fraction of incident diffuse radiation transmitted through the canopy. The ground albedo is represented as a snow-cover-weighted mixture,

$$\alpha_{\mathrm{g},\Lambda} = f_{\mathrm{snow}}\,\alpha_{\mathrm{snow},\Lambda} + (1 - f_{\mathrm{snow}})\,\alpha_{\mathrm{soil},\Lambda}, \tag{A4}$$

where f_{snow} is the snow cover fraction diagnosed from snow water storage (Sect. A5), and $\alpha_{\mathrm{snow},\Lambda}$ and $\alpha_{\mathrm{soil},\Lambda}$ are band-specific snow and soil albedos. The same blended albedo applies to direct-beam and diffuse radiation at the lower boundary.

The canopy shortwave absorption in each band follows by energy balance,

$$R^{\mathrm{n}}_{\mathrm{sw,v},\Lambda} = R^{\mu}_{\mathrm{sw},\Lambda} + R^{\mathrm{d}}_{\mathrm{sw},\Lambda} - \left(\alpha^{\mu}_{\Lambda} R^{\mu}_{\mathrm{sw},\Lambda} + \alpha^{\mathrm{d}}_{\Lambda} R^{\mathrm{d}}_{\mathrm{sw},\Lambda}\right) - R^{\mathrm{n}}_{\mathrm{sw,g},\Lambda}, \tag{A5}$$

where α^{μ}_{Λ} and $\alpha^{\mathrm{d}}_{\Lambda}$ are the effective top-of-canopy reflectance coefficients for direct-beam and diffuse radiation. The net shortwave components $R^{\mathrm{n}}_{\mathrm{sw,v}}$ and $R^{\mathrm{n}}_{\mathrm{sw,g}}$ used in Eq. (3) are the sums of these band-specific terms over Λ.

The reflectance coefficients $\alpha^{\mu}_{\Lambda}, \alpha^{\mathrm{d}}_{\Lambda}$ and the transmittance coefficients $f_{\mathrm{tdd},\Lambda}, f_{\mathrm{tid},\Lambda}, f_{\mathrm{tii},\Lambda}$ are obtained from the analytical two-stream solution and depend on the canopy single-scattering albedo, the upscatter parameters, the optical depth, the leaf-angle distribution, the vegetation amount, the solar geometry, and the ground albedo. For snow-free canopy elements the

https://doi.org/10.5194/egusphere-2026-3294
Preprint. Discussion started: 29 July 2026

single-scattering albedo is $\omega_{\Lambda,\mathrm{veg}} = \rho_{\Lambda,\mathrm{veg}} + \tau_{\Lambda,\mathrm{veg}}$, where $\rho_{\Lambda,\mathrm{veg}}$ and $\tau_{\Lambda,\mathrm{veg}}$ are the area-weighted reflectance and transmittance of leaf and stem elements. The upscatter parameters and optical depth follow the Sellers two-stream formulation (Sellers, 1985), with the leaf-angle projection $G(\mu_\mathrm{s})$ and the diffuse optical-depth term based on the polynomial leaf-angle parameterization of Campbell (1990). When snow is present on the canopy, the single-scattering albedo and upscatter parameters are blended between snow-free vegetation and snow values in proportion to the canopy snow fraction, with snow assumed to scatter isotropically.

The longwave intermediate fluxes are defined as follows. The downward longwave flux below the canopy combines atmospheric longwave transmitted through the canopy and canopy thermal emission,

$$R^{\downarrow}_{\mathrm{lw,v}} = (1 - \varepsilon_\mathrm{v})\, R^{\downarrow}_{\mathrm{lw}} + E_\mathrm{v}. \tag{A6}$$

The upward longwave flux from the ground combines reflected downward longwave and ground thermal emission,

$$R^{\uparrow}_{\mathrm{lw,g}} = (1 - \varepsilon_\mathrm{g})\, R^{\downarrow}_{\mathrm{lw,v}} + E_\mathrm{g}. \tag{A7}$$

The upward longwave flux leaving the canopy top combines ground-origin longwave transmitted through the canopy and canopy thermal emission,

$$R^{\uparrow}_{\mathrm{lw,vg}} = (1 - \varepsilon_\mathrm{v})\, R^{\uparrow}_{\mathrm{lw,g}} + E_\mathrm{v}. \tag{A8}$$

The emission terms are $E_\mathrm{v} = \varepsilon_\mathrm{v}\,\sigma\, T_\mathrm{v}^4$ and $E_\mathrm{g} = \varepsilon_\mathrm{g}\,\sigma\, T_\mathrm{g}^4$, where σ is the Stefan–Boltzmann constant. In ADELM v1.0, the surface temperatures (T_v and T_g) are approximated by air temperature (T_a), consistent with the daily time step and the absence of an explicit surface energy balance. The canopy emissivity is diagnosed from the vegetation area index as $\varepsilon_\mathrm{v} = 1 - \exp(-\mathrm{VAI})$ with $\mathrm{VAI} = \mathrm{LAI} + \mathrm{SAI}$, where LAI and SAI denote leaf area index and stem area index, respectively. The ground emissivity ε_g is prescribed separately for soil and snow surfaces.

The net longwave components entering Eq. (3) follow from these intermediate fluxes, with the sign convention that net values are positive when absorbed by the target surface,

$$R^{\mathrm{n}}_{\mathrm{lw,g}} = R^{\downarrow}_{\mathrm{lw,v}} - R^{\uparrow}_{\mathrm{lw,g}}, \tag{A9}$$

$$R^{\mathrm{n}}_{\mathrm{lw,v}} = R^{\downarrow}_{\mathrm{lw}} + R^{\uparrow}_{\mathrm{lw,g}} - R^{\downarrow}_{\mathrm{lw,v}} - R^{\uparrow}_{\mathrm{lw,vg}}. \tag{A10}$$

The absorbed photosynthetically active radiation $\mathrm{APAR_{leaf}}$ passed to $\mathcal{M}_\mathrm{photo}$ (Sect. A3) is obtained by multiplying the net canopy visible-band absorption $R^{\mathrm{n}}_{\mathrm{sw,v,vis}}$ by $\mathrm{LAI}/\mathrm{VAI}$.

A2 Soil hydraulics module $\mathcal{M}_{\mathbf{hydra}}$

This appendix details the root fraction $f_{\mathrm{root},i}$, the hydraulic conductivity K_i, and the soil water potential $\psi_{\mathrm{soil},i}$ that enter the layer-wise plant water supply in Eq. (4), together with the fallback used when the total supply across the column is zero.

The root fraction follows an exponential vertical profile (Jackson et al., 1996),

$$f_{\mathrm{root},i} = \frac{r_i}{\sum_j r_j}, \qquad r_i = \beta^{z_{\mathrm{top},i}} - \beta^{z_{\mathrm{bot},i}}, \tag{A11}$$

https://doi.org/10.5194/egusphere-2026-3294
Preprint. Discussion started: 29 July 2026

where $z_{\mathrm{top},i}$ and $z_{\mathrm{bot},i}$ are the upper and lower depths of layer i in centimetres, and β is a root distribution shape parameter. Smaller β places a larger fraction of roots near the surface, and values closer to one give a deeper profile.

The hydraulic conductivity K_i available for plant water supply is diagnosed from the current liquid soil moisture through a power-law relationship (Campbell, 1974),

$$K_i = f_{\mathrm{freeze}}\, K_{\mathrm{sat},i} \left(\frac{\theta_i}{\theta_{\mathrm{sat},i}}\right)^{3+2B_i}, \tag{A12}$$

where $K_{\mathrm{sat},i}$ is the saturated hydraulic conductivity, θ_i is the volumetric moisture content of layer i, $\theta_{\mathrm{sat},i}$ is the saturated volumetric moisture content, B_i is the retention-curve slope parameter defined below, and f_{freeze} is a smooth factor that reduces plant-supply conductivity as temperature falls toward freezing. The freeze reduction applies only to plant-supply conductivity; gravitational drainage suppression instead uses a temperature threshold in Sect. A5. The saturated parameters $K_{\mathrm{sat},i}$ and $\theta_{\mathrm{sat},i}$ are obtained from soil texture through the Saxton–Rawls pedotransfer relationships (Saxton and Rawls, 2006), with $K_{\mathrm{sat},i}$ converted to $\mathrm{mm\,d^{-1}}$ for use at the daily time step.

The soil water potential $\psi_{\mathrm{soil},i}$ is diagnosed from a piecewise retention curve. Below field capacity the curve follows the Campbell power-law form (Campbell, 1974), and above field capacity it is interpolated linearly toward near-saturation for numerical continuity,

$$\psi_{\mathrm{soil},i} = \begin{cases} A_i\, \theta_i^{-B_i}, & \theta_i \le \theta_{\mathrm{fc},i}, \\ \psi_{\mathrm{fc}} + \dfrac{(\theta_i - \theta_{\mathrm{fc},i})(\psi_{\mathrm{e},i} - \psi_{\mathrm{fc}})}{\theta_{\mathrm{sat},i} - \theta_{\mathrm{fc},i}}, & \theta_i > \theta_{\mathrm{fc},i}, \end{cases} \tag{A13}$$

where $\theta_{\mathrm{fc},i}$ is the field-capacity water content, $\psi_{\mathrm{fc}} = -0.033$ MPa is the fixed field-capacity water potential, and $\psi_{\mathrm{e},i}$ is the air-entry water potential. The coefficients A_i and B_i of the dry branch are determined by requiring that the curve pass through the field-capacity and wilting-point ($\theta_{\mathrm{wp},i}$) reference points. The dry branch represents the nonlinear decrease in water potential as the soil dries, and the wet branch provides a smooth transition between field capacity and near-saturation conditions.

When the total supply across the column is zero, the normalized uptake fractions $\zeta_i = S_i / \sum_j S_j$ entering Eq. (4) are undefined. In that case the fractions fall back to a unit weight on the top soil layer so that ψ_{root} remains defined for the stomatal regulation in $\mathcal{M}_{\mathrm{photo}}$ (Sect. A3). Transpiration withdrawals are independently limited to zero by the water available in each layer in $\mathcal{M}_{\mathrm{wb}}$ (Sect. A5).

A3 Photosynthesis module $\mathcal{M}_{\mathrm{photo}}$

This appendix details the canopy stomatal conductance $g_{\mathrm{s,can}}$, the canopy CO_2 conductance $g_{\mathrm{c,CO_2}}$, and the internal canopy CO_2 concentration $C_{\mathrm{i,can}}$ that enter the diffusion-limited uptake rate A_{d} in Eq. (5).

The leaf stomatal conductance follows a Jarvis multiplicative scheme (Jarvis, 1976),

$$g_{\mathrm{s,leaf}} = g_{\mathrm{s,min}} + (g_{\mathrm{s,max}} - g_{\mathrm{s,min}})\, f_{\mathrm{gs}}, \qquad f_{\mathrm{gs}} = f_{\mathrm{rad}}\, f_{\mathrm{temp}}\, f_{\mathrm{vpd}}\, f_{\psi}, \tag{A14}$$

where $g_{\mathrm{s,min}}$ and $g_{\mathrm{s,max}}$ are the prescribed minimum and maximum stomatal conductances, and the four response factors describe the response of stomatal conductance to incident radiation, air temperature, vapor pressure deficit, and root-zone soil

https://doi.org/10.5194/egusphere-2026-3294
Preprint. Discussion started: 29 July 2026

water potential, respectively. The radiation response is

$$f_{\mathrm{rad}} = \frac{\mathrm{PAR_{in}}}{\mathrm{PAR_{in}} + \mathrm{PAR}_{1/2}}, \tag{A15}$$

where $\mathrm{PAR_{in}}$ is the visible-band downwelling flux at the canopy top before interception and $\mathrm{PAR}_{1/2}$ is the half-saturation parameter. The temperature response is

$$f_{\mathrm{temp}} = 1 - a_T (T_{\mathrm{opt,gs}} - T_{\mathrm{a}})^2, \tag{A16}$$

where $T_{\mathrm{opt,gs}}$ is the stomatal optimum temperature and a_T is a curvature parameter. The vapor pressure deficit response is

$$f_{\mathrm{vpd}} = \frac{1}{1 + k_{\mathrm{vpd}}\,\mathrm{VPD}}, \tag{A17}$$

where k_{vpd} controls stomatal sensitivity to vapor pressure deficit. The water-stress response is

$$f_{\psi} = \frac{1}{1 + \exp[-k_{\psi}(\psi_{\mathrm{root}} - \psi_{\mathrm{soil,50}})]}, \tag{A18}$$

where ψ_{root} is supplied by $\mathcal{M}_{\mathrm{hydra}}$ (Sect. A2), $\psi_{\mathrm{soil,50}}$ is the soil water potential at half-maximum conductance, and k_{ψ} controls the steepness of the response.

The canopy stomatal conductance scales the leaf value by an effective leaf area index (Zhang et al., 2008),

$$g_{\mathrm{s,can}} = \mathrm{LAI_{eff}}\, g_{\mathrm{s,leaf}}, \tag{A19}$$

where $\mathrm{LAI_{eff}}$ accounts for the diminishing contribution of deeply shaded leaves to bulk canopy conductance. It equals the actual LAI for $\mathrm{LAI} \le 2$, equals $0.5\,\mathrm{LAI}$ for $\mathrm{LAI} \ge 4$, and is fixed at 2 for intermediate values.

The canopy CO_2 conductance $g_{\mathrm{c,CO_2}}$ combines the canopy stomatal conductance with the leaf boundary-layer conductance $g_{\mathrm{b}} = 1/r_{\mathrm{b}}$ and the above-canopy aerodynamic conductance $g_{\mathrm{a}} = 1/r_{\mathrm{a}}$ in series, converted to a CO_2 molar basis by accounting for the molecular diffusivity ratio of water vapor and CO_2. The resistance forms r_{b} and r_{a} are common to the transpiration pathway of $\mathcal{M}_{\mathrm{et}}$ and are given in Sect. A4.

The internal canopy CO_2 concentration $C_{\mathrm{i,can}}$ is diagnosed by equating the diffusive CO_2 supply with a Farquhar-type capacity response,

$$C_{\mathrm{i,can}}^2 + \left(\frac{A_{\mathrm{can}}}{g_{\mathrm{c,CO_2}}} - C_{\mathrm{a}} + K_{\mathrm{m}}\right) C_{\mathrm{i,can}} - C_{\mathrm{a}} K_{\mathrm{m}} - \frac{A_{\mathrm{can}}}{g_{\mathrm{c,CO_2}}} \Gamma^* = 0, \tag{A20}$$

taking the positive root, where Γ^* is the photorespiratory CO_2 compensation point and K_{m} is the apparent CO_2 half-saturation constant accounting for competitive O_2 inhibition. The canopy photosynthetic capacity entering this quadratic is

$$A_{\mathrm{can}} = \mathrm{LAI}\, A_{\mathrm{cap}}\, f_{T,\mathrm{cap}}(T_{\mathrm{a}}), \tag{A21}$$

where A_{cap} is a photosynthetic capacity coefficient and $f_{T,\mathrm{cap}}$ is a peaked temperature response with optimum temperature $T_{\mathrm{opt,cap}}$ and upper-limit temperature $T_{\mathrm{max,cap}}$. The temperature dependencies of Γ^*, K_c, K_o, and hence of K_{m}, follow Arrhenius-type functions with reference values and activation parameters from Bernacchi et al. (2001).

https://doi.org/10.5194/egusphere-2026-3294
Preprint. Discussion started: 29 July 2026

A4 Evapotranspiration module $\mathcal{M}_{\mathrm{et}}$

This appendix details the pathway-specific values of $R_{\mathrm{n},j}$, $r_{\mathrm{a},j}$, $r_{\mathrm{s},j}$, Δe_j, Δ_j, λ_j, γ_j that specialize the general Penman–Monteith form (see Eq. (6)) to the five pathways, together with the resistance and vapor pressure forms underlying them.

For the transpiration pathway ($j = \mathrm{tr}$), the net radiation is the canopy net radiation $R_{\mathrm{n,v}}$, the aerodynamic resistance is the above-canopy resistance r_{a}, the surface resistance is the sum of the canopy stomatal resistance r_{c} and the leaf boundary-layer resistance r_{b}, and the vapor pressure gradient is the atmospheric vapor pressure deficit, $\Delta e_{\mathrm{tr}} = \mathrm{VPD}$. The molar canopy conductance $g_{\mathrm{s,can}}$ supplied by $\mathcal{M}_{\mathrm{photo}}$ (Sect. A3) is converted to the resistance entering Eq. (6) through $r_{\mathrm{c}} = \rho_{\mathrm{mol}}/g_{\mathrm{s,can}}$, where $\rho_{\mathrm{mol}} = p_{\mathrm{a}}/(RT_K)$ is the molar density of air.

For the wet-canopy evaporation pathway ($j = \text{can-liq}$), the canopy net radiation $R_{\mathrm{n,v}}$ and above-canopy resistance r_{a} apply as for transpiration, the surface resistance reduces to the leaf boundary-layer resistance alone, $r_{\mathrm{s,can\text{-}liq}} = r_{\mathrm{b}}$, since there is no stomatal regulation of evaporation from wet leaf surfaces, and the vapor pressure gradient is $\Delta e_{\mathrm{can\text{-}liq}} = \mathrm{VPD}$.

For the soil evaporation pathway ($j = \mathrm{soil}$), the net radiation is the ground net radiation $R_{\mathrm{n,g}}$, the aerodynamic resistance is the soil aerodynamic resistance $r_{\mathrm{a,soil}}$, the surface resistance is the soil surface resistance r_{ss}, and the vapor pressure gradient is the soil-to-air vapor pressure gradient Δe_{soil} defined below.

For the ground-snow sublimation pathway ($j = \mathrm{snow}$), the net radiation is $R_{\mathrm{n,g}}$ and the aerodynamic resistance is $r_{\mathrm{a,soil}}$, with zero surface resistance and an ice-phase vapor pressure gradient $\Delta e_{\mathrm{ice}} = e_{\mathrm{sat,ice}}(T_{\mathrm{a}}) - e_{\mathrm{a}}$, where $e_{\mathrm{sat,ice}}$ is the saturation vapor pressure over ice. The slope and latent heat in Eq. (6) are replaced by their ice-phase counterparts Δ_{ice} and λ_{s}, and the psychrometric constant is rescaled as $\gamma_{\mathrm{s}} = \gamma\,\lambda_{\mathrm{v}}/\lambda_{\mathrm{s}}$.

For the canopy-snow sublimation pathway ($j = \mathrm{sub}$), ADELM v1.0 adopts a simplified treatment in which only the latent heat is taken in its ice-phase form, and the wet-canopy evaporation demand is rescaled by the latent heat ratio,

$$E_{\mathrm{sub,pot}} = E_{\mathrm{can\text{-}liq,pot}}\,\frac{\lambda_{\mathrm{v}}}{\lambda_{\mathrm{s}}}. \tag{A22}$$

The above-canopy aerodynamic resistance r_{a} governs vapor exchange between the canopy and the atmosphere. The displacement height d and roughness length z_0 are diagnosed from canopy height h_{c} and leaf area index following standard canopy aerodynamic relationships (Choudhury and Monteith, 1988; Sellers et al., 1996), and the friction velocity is $u_* = C_u\,u$, where u is the wind speed and C_u is a dimensionless wind-to-friction-velocity factor that increases with leaf area index. Two regimes apply depending on canopy height. For tall canopies ($h_{\mathrm{c}} > 3$ m), the wind speed is extrapolated to a reference height of 50 m through an open-field logarithmic profile, and r_{a} integrates an exponential wind-decay region within the canopy, a mixing-layer transition, and a logarithmic outer layer,

$$r_{\mathrm{a}} = \frac{\ln\left(\dfrac{z_{\mathrm{ref}} - d}{z_0}\right)}{k^2\,u_{\mathrm{ref}}}\left[\frac{h_{\mathrm{c}}}{a_w(Z_w - d)}\left(e^{a_w\left(1 - \frac{d + z_0}{h_c}\right)} - 1\right) + \frac{Z_w - h_{\mathrm{c}}}{Z_w - d} + \ln\left(\frac{z_{\mathrm{ref}} - d}{Z_w - d}\right)\right], \tag{A23}$$

where k is the von Kármán constant, a_w is the within-canopy wind attenuation coefficient, Z_w is the mixing-layer transition height, z_{ref} is the reference height, and u_{ref} is the wind speed extrapolated to z_{ref}. For short canopies ($h_{\mathrm{c}} \le 3$ m), r_{a} follows a double-logarithm form referenced to an effective height set by the displacement height.

https://doi.org/10.5194/egusphere-2026-3294
Preprint. Discussion started: 29 July 2026

The soil aerodynamic resistance $r_{\mathrm{a,soil}}$ governs vapor transport between the soil surface and the canopy air space. It is obtained by integrating an exponential within-canopy wind profile characterized by a decay coefficient that increases with leaf area index,

$$\eta = \sqrt{\frac{c_f\, h_\mathrm{c}\, \mathrm{LAI}}{l_m}}, \tag{A24}$$

where c_f is a foliage drag coefficient and l_m is a within-canopy mixing length that scales with canopy height and leaf area index. Integrating the eddy diffusivity profile between the soil and the base of the above-canopy layer gives

$$r_{\mathrm{a,soil}} = \frac{h_\mathrm{c}}{\eta K_h}\left[\exp\left(\eta\left(1-\frac{z_{0,\mathrm{soil}}}{h_\mathrm{c}}\right)\right) - \exp\left(\eta\left(1-\frac{z_0+d}{h_\mathrm{c}}\right)\right)\right], \tag{A25}$$

where K_h is the eddy diffusivity at the canopy top and $z_{0,\mathrm{soil}}$ is the soil roughness length.

The leaf boundary-layer resistance $r_\mathrm{b} = 1/g_\mathrm{b}$ governs exchange between leaf surfaces and the canopy air space. The conductance follows a Sherwood-number relationship for forced convection at the leaf surface,

$$g_\mathrm{b} = c_b\, \mathrm{LAI}\, \frac{D_\mathrm{leaf}}{d_\mathrm{leaf}}\, \mathrm{Re}^{1/2}, \qquad \mathrm{Re} = \frac{u_\mathrm{c}\, d_\mathrm{leaf}}{\nu}, \tag{A26}$$

where D_leaf is the molecular diffusivity of water vapor, d_leaf is the characteristic leaf dimension, ν is the kinematic viscosity of air, u_c is a representative within-canopy wind speed, Re is the leaf-scale Reynolds number, and c_b collects the empirical constants of the Sherwood relationship.

The soil surface resistance r_ss increases as the surface dries through a Sellers-type form (Sellers et al., 1992),

$$r_\mathrm{ss} = f_\mathrm{snow}\, r_\mathrm{snow,min} + (1 - f_\mathrm{snow})\, \exp\left(8.25 - k_\mathrm{ss}\, \frac{\theta_1}{\theta_{\mathrm{sat},1}}\right), \tag{A27}$$

where θ_1 and $\theta_{\mathrm{sat},1}$ are the volumetric and saturated moisture contents of the top soil layer (Sect. A2), f_snow is the snow cover fraction (Sect. A5), $r_\mathrm{snow,min}$ is a low resistance assigned to the snow-covered fraction, and k_ss is a moisture sensitivity parameter. The snow-covered fraction is assigned a low resistance because its vapor flux is represented separately by the ground-snow sublimation pathway, so soil evaporation is evaluated only after accounting for ground-snow sublimation.

The vapor pressure at the soil surface is reduced below saturation through the Kelvin relation,

$$e_\mathrm{s,soil} = e_\mathrm{sat}(T_K)\, \exp\left(\frac{V_w\, \psi_{\mathrm{soil},1}}{R T_K}\right), \tag{A28}$$

where V_w is the molar volume of liquid water, R is the universal gas constant, $\psi_{\mathrm{soil},1}$ is the top-layer soil water potential (Sect. A2) expressed in pascals, and T_K is air temperature in kelvin. The soil-to-air vapor pressure gradient is $\Delta e_\mathrm{soil} = \max(e_\mathrm{s,soil} - e_\mathrm{a}, 0)$.

A5 Snow and soil hydrology module $\mathcal{M}_\mathrm{wb}$

This appendix details the forcing and loss terms entering the bucket updates Eqs. (7)–(9) and the layer-wise mass conservation Eq. (10), together with the snow cover fraction f_snow used by other modules. All fluxes in this section are water depths integrated over the daily time step.

https://doi.org/10.5194/egusphere-2026-3294
Preprint. Discussion started: 29 July 2026

Precipitation phase is determined from the fraction of the day during which air temperature exceeds the freeze threshold T_{freeze}, assuming a linear diurnal temperature variation between the daily minimum $T_{\mathrm{a,min}}$ and maximum $T_{\mathrm{a,max}}$,

$$f_{\mathrm{warm}} = \begin{cases} 0, & T_{\mathrm{a,max}} \leq T_{\mathrm{freeze}}, \\ 1, & T_{\mathrm{a,min}} \geq T_{\mathrm{freeze}}, \\ \dfrac{T_{\mathrm{a,max}} - T_{\mathrm{freeze}}}{T_{\mathrm{a,max}} - T_{\mathrm{a,min}}}, & \text{otherwise.} \end{cases} \tag{A29}$$

Rainfall and atmospheric snowfall are then $P_{\mathrm{rain}} = f_{\mathrm{warm}}\,P$ and $P_{\mathrm{snow,atm}} = (1 - f_{\mathrm{warm}})\,P$, where P is the total daily precipitation.

The liquid canopy interception input is the rainfall, $I_{\mathrm{can,liq}} = P_{\mathrm{rain}}$, and the liquid interception capacity scales with LAI as $W_{\mathrm{can,liq,max}} = c_{\mathrm{liq}}\,\mathrm{LAI}$, where c_{liq} is the liquid interception capacity coefficient. The drip flux in Eq. (7) is the rainfall in excess of the remaining capacity,

$$D_{\mathrm{can,liq}} = \max(W_{\mathrm{can,liq}} + I_{\mathrm{can,liq}} - W_{\mathrm{can,liq,max}},\, 0)\,, \tag{A30}$$

and the actual wet-canopy evaporation is limited by the available storage,

$$E_{\mathrm{can,liq}} = \min(E_{\mathrm{can,liq,pot}},\, W_{\mathrm{can,liq}})\,, \tag{A31}$$

with $E_{\mathrm{can,liq,pot}}$ supplied by $\mathcal{M}_{\mathrm{et}}$ (Sect. A4).

The solid canopy interception input is the intercepted fraction of atmospheric snowfall, $I_{\mathrm{can,sol}} = f_{\mathrm{int}}\,P_{\mathrm{snow,atm}}$, where $f_{\mathrm{int}} = 1 - \exp(-k_{\mathrm{int}}\,\mathrm{VAI})$ is the Beer-law interception fraction and k_{int} is an interception coefficient. The solid interception capacity scales with VAI as $W_{\mathrm{can,sol,max}} = c_{\mathrm{snow}}\,\mathrm{VAI}$, where c_{snow} is the solid interception capacity coefficient. Canopy snow sublimation is limited by the available storage,

$$E_{\mathrm{sub}} = \min(E_{\mathrm{sub,pot}},\, W_{\mathrm{can,sol}})\,, \tag{A32}$$

and the unloading flux in Eq. (8) carries any excess over capacity to the ground after accounting for sublimation,

$$D_{\mathrm{can,sol}} = \max(W_{\mathrm{can,sol}} + I_{\mathrm{can,sol}} - E_{\mathrm{sub}} - W_{\mathrm{can,sol,max}},\, 0)\,. \tag{A33}$$

The snowfall reaching the ground in Eq. (9) is the non-intercepted fraction of atmospheric snowfall, $P_{\mathrm{snow}} = (1 - f_{\mathrm{int}})\,P_{\mathrm{snow,atm}}$, so that the total snow input to the ground store is $P_{\mathrm{snow}} + D_{\mathrm{can,sol}}$. The snow cover fraction is diagnosed from ground snow water storage as

$$f_{\mathrm{snow}} = \frac{W_{\mathrm{snow}}}{W_{\mathrm{snow}} + W_{\mathrm{scale}}}, \tag{A34}$$

where W_{scale} controls how rapidly fractional snow cover approaches unity with increasing snow water storage. Actual ground-snow sublimation is scaled by the snow cover fraction and bounded by the available snow water,

$$E_{\mathrm{snow}} = \min(f_{\mathrm{snow}}\,E_{\mathrm{snow,pot}},\, W_{\mathrm{snow}})\,, \tag{A35}$$

https://doi.org/10.5194/egusphere-2026-3294
Preprint. Discussion started: 29 July 2026

and snowmelt follows a degree-day formulation bounded by the available snow water,

$$M = \min(c_{\mathrm{melt}}\, \max(T_{\mathrm{a}} - T_{\mathrm{freeze}}, 0),\, W_{\mathrm{snow}})\,, \tag{A36}$$

where c_{melt} is the degree-day melt coefficient.

Liquid water reaching the soil surface combines canopy drip and snowmelt, $P_{\mathrm{liq,surf}} = D_{\mathrm{can,liq}} + M$. This input is partitioned into infiltration and surface runoff through a sub-grid soil capacity curve over the runoff-generation layers, following the variable-infiltration concept of Liang et al. (1994). The maximum infiltration capacity is $I_{\mathrm{cap,max}} = (1 + b_{\mathrm{inf}})\, W_{\mathrm{run,max}}$, where $W_{\mathrm{run,max}}$ is the total pore space of the runoff-generation layers and b_{inf} is a shape parameter controlling sub-grid heterogeneity. The position on the capacity curve at the start of the time step, $W_{\mathrm{cap},0}$, is obtained by inverting this curve from the current relative wetness $W_{\mathrm{run}}/W_{\mathrm{run,max}}$. The incremental infiltration is

$$W_{\mathrm{inf}} = W_{\mathrm{run,max}} \left[1 - \left(1 - \frac{W_{\mathrm{cap},0} + P_{\mathrm{liq,surf}}}{I_{\mathrm{cap,max}}} \right)^{1+b_{\mathrm{inf}}} \right] - W_{\mathrm{run}}, \tag{A37}$$

and surface runoff is the residual, $Q_{\mathrm{surf}} = P_{\mathrm{liq,surf}} - W_{\mathrm{inf}}$. When $W_{\mathrm{cap},0} + P_{\mathrm{liq,surf}} \geq I_{\mathrm{cap,max}}$, the runoff-generation layers fill to capacity and all remaining liquid water becomes surface runoff.

Soil evaporation and ground-snow sublimation draw on the same ground vapor flux. The realized soil evaporation reduces the potential demand by the already-realized snow sublimation and is limited by available top-layer water,

$$E_{\mathrm{soil}} = \min\big(\max(E_{\mathrm{soil,pot}} - E_{\mathrm{snow}}, 0),\, W^{\mathrm{avail}}_{\mathrm{soil},1}\big)\,, \tag{A38}$$

where $W^{\mathrm{avail}}_{\mathrm{soil},1}$ is the top-layer storage available for evaporation. Transpiration is distributed across layers using the uptake fractions ζ_i from $\mathcal{M}_{\mathrm{hydra}}$ (Sect. A2), and each layer withdrawal is limited by available water,

$$E_{\mathrm{tr},i} = \min\big(\zeta_i\, E_{\mathrm{tr,pot}},\, W^{\mathrm{avail}}_{\mathrm{soil},i}\big)\,, \qquad E_{\mathrm{tr}} = \sum_i E_{\mathrm{tr},i}, \tag{A39}$$

where $W^{\mathrm{avail}}_{\mathrm{soil},i}$ is the layer-i storage available for transpiration.

The interfacial flux Q_i in Eq. (10) represents gravity-driven drainage from layer i to layer $i+1$, with $Q_0 = W_{\mathrm{inf}}$ the surface infiltration. Drainage is gravity-driven under a unit-hydraulic-gradient assumption, so the Darcy flux equals the unsaturated conductivity $K(\theta_i)$ (Sect. A2). It acts only on moisture held above field capacity $\theta_{\mathrm{fc},i}$ and is inactive under freezing conditions (taken here as $T_{\mathrm{a}} < T_{\mathrm{freeze}}$),

$$Q_i = \min\big(K(\theta_i)\, \Delta t,\, (\theta_i - \theta_{\mathrm{fc},i})^+\, \Delta z_i\big)\,, \tag{A40}$$

where $(\cdot)^+$ denotes the positive part. The flux Q_n from the bottom layer constitutes the subsurface outflow. Capillary rise and lateral redistribution are not represented in ADELM v1.0.

Appendix B: Eddy covariance sites

The 63 eddy covariance sites used for model training and evaluation are listed in Table B1. The flux data products follow the source product recorded in PLUMBER2 (Ukkola et al., 2022), ICOS Warm Winter 2020 (Warm Winter 2020 Team and ICOS

https://doi.org/10.5194/egusphere-2026-3294
Preprint. Discussion started: 29 July 2026

Ecosystem Thematic Centre, 2020), and ICOS Drought-2018 (Drought 2018 Team and ICOS Ecosystem Thematic Centre, 2020). All sites are retained as natural or semi-natural vegetation classes and screened for gridded forcing and LAI availability as described in Sect. 3.1.

Appendix C: Parameter sources and prescribed baseline values

Model parameters fall into three baseline specification types. Scalar prescribed parameters (Table C1) use default values applied uniformly across all locations unless they are opened to learning in a parameterization experiment. PFT-based parameters (Table C2) are computed as plant-functional-type-fraction-weighted averages from lookup tables and vary with vegetation composition. Derived soil hydraulic parameters (Table C3) are computed layer-wise from soil texture, organic matter, and bulk density using pedotransfer functions (Saxton and Rawls, 2006).

Author contributions. S.J.: Conceptualization, Methodology, Validation, Formal analysis, Resources, Data curation, Writing – original draft, Writing – review and editing, Visualization, Supervision, Project administration, Funding acquisition. G.B.: Conceptualization, Methodology, Validation, Writing – review and editing. T.W.: Methodology, Validation, Writing – review and editing. Y.Z.: Writing – review and editing. J.Z.: Methodology, Validation, Writing – review and editing.

Competing interests. The authors declare that they have no conflict of interest.

Acknowledgements. This research was supported by the Carl-Zeiss-Stiftung through the Junior Research Group *Knowledge Integration for Spatio-Temporal Environmental Modeling* (P2021-00-008) and the CZS Breakthroughs project GENAI-X (P2024-11-042). The authors thank Chao Wang for developing an early prototype that supported the initial model development.

https://doi.org/10.5194/egusphere-2026-3294
Preprint. Discussion started: 29 July 2026

Table B1. Eddy covariance sites used for model training and evaluation. IGBP land-cover classes are defined as in Fig. 4.

Site ID	Site name	Data product	Latitude	Longitude	IGBP	Years
AT-Neu	Neustift	PLUMBER2	47.12	11.32	GRA	2002–2012
BE-Bra	Brasschaat	ICOS-WW2020	51.31	4.52	MF	1996–2020
BE-Dor	Dorinne	ICOS-WW2020	50.31	4.97	GRA	2011–2020
BE-Lcr	Lochristi	ICOS-WW2020	51.10	3.85	DBF	2019–2020
BE-Maa	Maasmechelen	ICOS-WW2020	50.98	5.63	CSH	2016–2020
BE-Vie	Vielsalm	ICOS-WW2020	50.30	6.00	MF	1996–2020
CH-Aws	Alp Weissenstein	ICOS-WW2020	46.58	9.79	GRA	2006–2020
CH-Cha	Chamau	ICOS-WW2020	47.21	8.41	GRA	2005–2020
CH-Dav	Davos	ICOS-WW2020	46.82	9.86	ENF	1997–2020
CH-Fru	Früebüel	ICOS-WW2020	47.12	8.54	GRA	2005–2020
CH-Lae	Laegern	ICOS-WW2020	47.48	8.37	MF	2004–2020
CH-Oe1	Oensingen grassland	PLUMBER2	47.29	7.73	GRA	2002–2008
CZ-BK1	Bily Kriz forest	ICOS-WW2020	49.50	18.54	ENF	2004–2020
CZ-Lnz	Lanzhot	ICOS-WW2020	48.68	16.95	MF	2015–2020
CZ-RAJ	Rajec	ICOS-WW2020	49.44	16.70	ENF	2012–2020
CZ-Stn	Stitna	ICOS-WW2020	49.04	17.97	DBF	2010–2020
DE-Gri	Grillenburg	ICOS-WW2020	50.95	13.51	GRA	2004–2020
DE-Hai	Hainich	ICOS-WW2020	51.08	10.45	DBF	2000–2020
DE-HoH	Hohes Holz	ICOS-WW2020	52.09	11.22	DBF	2015–2020
DE-Hzd	Hetzdorf	ICOS-WW2020	50.96	13.49	DBF	2010–2020
DE-Obe	Oberbärenburg	ICOS-WW2020	50.79	13.72	ENF	2008–2020
DE-RuR	Rollesbroich	ICOS-WW2020	50.62	6.30	GRA	2011–2020
DE-RuW	Wustebach	ICOS-WW2020	50.50	6.33	ENF	2012–2020
DE-Tha	Tharandt	ICOS-WW2020	50.96	13.57	ENF	1996–2020
DK-Gds	Gludsted Plantage	ICOS-WW2020	56.07	9.33	ENF	2020
DK-Sor	Soroe	ICOS-WW2020	55.49	11.64	DBF	1996–2020
ES-Abr	Albuera	ICOS-WW2020	38.70	-6.79	SAV	2015–2020
ES-Agu	Aguamarga	ICOS-WW2020	36.94	-2.03	OSH	2006–2020
ES-Cnd	Conde	ICOS-WW2020	37.91	-3.23	WSA	2014–2020
ES-LJu	Llano de los Juanes	ICOS-WW2020	36.93	-2.75	OSH	2004–2020
ES-LM1	Majadas del Tietar North	ICOS-WW2020	39.94	-5.78	SAV	2014–2020
ES-LM2	Majadas del Tietar South	ICOS-WW2020	39.94	-5.78	SAV	2014–2020
ES-LgS	Laguna Seca	PLUMBER2	37.10	-2.97	OSH	2007

https://doi.org/10.5194/egusphere-2026-3294
Preprint. Discussion started: 29 July 2026

Table B1. Eddy covariance sites used for model training and evaluation. Continued.

Site ID	Site name	Data product	Latitude	Longitude	IGBP	Years
FI-Hyy	Hyytiälä	ICOS-WW2020	61.85	24.29	ENF	1996–2020
FI-Ken	Kenttarova	ICOS-WW2020	67.99	24.24	ENF	2018–2020
FI-Let	Lettosuo	ICOS-WW2020	60.64	23.96	ENF	2009–2020
FI-Sod	Sodankyla	PLUMBER2	67.36	26.64	ENF	2008–2014
FI-Var	Varrio	ICOS-WW2020	67.75	29.61	ENF	2016–2020
FR-Bil	Bilos	ICOS-WW2020	44.49	-0.96	ENF	2014–2020
FR-Fon	Fontainebleau-Barbeau	ICOS-WW2020	48.48	2.78	DBF	2005–2020
FR-Hes	Hesse	PLUMBER2	48.67	7.07	DBF	1997–2006
FR-LBr	Le Bray	PLUMBER2	44.72	-0.77	ENF	2003–2008
FR-Pue	Puechabon	PLUMBER2	43.74	3.60	EBF	2000–2014
FR-Tou	Toulouse	ICOS-WW2020	43.57	1.37	GRA	2018–2020
IT-BFt	Bosco Fontana	ICOS-WW2020	45.20	10.74	DBF	2019–2020
IT-CA1	Castel d'Asso1	PLUMBER2	42.38	12.03	DBF	2012–2013
IT-CA3	Castel d'Asso 3	PLUMBER2	42.38	12.02	DBF	2012–2013
IT-Col	Collelongo	PLUMBER2	41.85	13.59	DBF	2007–2014
IT-Isp	Ispra ABC-IS	PLUMBER2	45.81	8.63	DBF	2013–2014
IT-Lav	Lavarone	ICOS-WW2020	45.96	11.28	ENF	2003–2020
IT-Lsn	Lison	ICOS-WW2020	45.74	12.75	OSH	2016–2020
IT-MBo	Monte Bondone	ICOS-WW2020	46.01	11.05	GRA	2003–2020
IT-PT1	Parco Ticino forest	PLUMBER2	45.20	9.06	DBF	2003–2004
IT-Ren	Renon	ICOS-WW2020	46.59	11.43	ENF	1999–2020
IT-Ro1	Roccarespampani 1	PLUMBER2	42.41	11.93	DBF	2002–2006
IT-Ro2	Roccarespampani 2	PLUMBER2	42.39	11.92	DBF	2002–2008
IT-Tor	Torgnon	ICOS-WW2020	45.84	7.58	GRA	2008–2020
NL-Hor	Horstermeer	PLUMBER2	52.24	5.07	GRA	2008–2011
NL-Loo	Loobos	ICOS-Drought2018	52.17	5.74	ENF	1996–2018
SE-Htm	Hyltemossa	ICOS-WW2020	56.10	13.42	ENF	2015–2020
SE-Nor	Norunda	ICOS-WW2020	60.09	17.48	ENF	2014–2020
SE-Ros	Rosinedal-3	ICOS-WW2020	64.17	19.74	ENF	2014–2020
SE-Svb	Svartberget	ICOS-WW2020	64.26	19.77	ENF	2014–2020

https://doi.org/10.5194/egusphere-2026-3294
Preprint. Discussion started: 29 July 2026

Table C1. Scalar prescribed baseline parameters of ADELM v1.0.

Module	Symbol	Parameter	Unit	Value
Radiative transfer	f_{vis}	VIS fraction of shortwave radiation	–	0.5
	f_{dir}	Direct-beam fraction	–	0.5
	$\alpha_{\mathrm{soil,vis}}$	Soil VIS albedo	–	0.15
	$\alpha_{\mathrm{soil,nir}}$	Soil NIR albedo	–	0.29
	$\alpha_{\mathrm{snow,vis}}$	Snow VIS albedo	–	0.95
	$\alpha_{\mathrm{snow,nir}}$	Snow NIR albedo	–	0.65
	ε_{g}	Soil/snow emissivity	–	0.96
Photosynthesis	$g_{\mathrm{s,max}}$	Maximum stomatal conductance	$\mathrm{mmol\,m^{-2}\,s^{-1}}$	500.0
	$g_{\mathrm{s,min}}$	Minimum stomatal conductance	$\mathrm{mmol\,m^{-2}\,s^{-1}}$	10.0
	$T_{\mathrm{opt,gs}}$	Stomatal temperature optimum	$^{\circ}\mathrm{C}$	25.0
	a_T	Temperature curvature	$^{\circ}\mathrm{C}^{-2}$	0.0016
	$\psi_{\mathrm{soil,50}}$	Soil water potential at half-max g_{s}	MPa	-0.3
	k_{ψ}	Water stress steepness	MPa^{-1}	3.0
	ϵ_{L}	Light-use efficiency	$\mathrm{gC\,MJ^{-1}}$	1.2
	A_{cap}	Photosynthetic capacity coefficient	$\mathrm{gC\,m^{-2}\,leaf\,d^{-1}}$	25.0
	$T_{\mathrm{opt,cap}}$	Photosynthetic capacity optimum temperature	$^{\circ}\mathrm{C}$	30.0
	$T_{\mathrm{max,cap}}$	Photosynthetic capacity upper-limit temperature	$^{\circ}\mathrm{C}$	56.0
	θ_{co}	Photosynthesis co-limitation curvature	–	0.95
Evapotranspiration	k_{ss}	Soil surface resistance moisture sensitivity	–	4.225
	$z_{0,\mathrm{soil}}$	Soil aerodynamic roughness length	m	0.01
Snow and soil hydrology	c_{liq}	Liquid interception capacity coefficient	mm	0.2
	c_{snow}	Solid interception capacity coefficient	mm	1.0
	c_{melt}	Degree-day melt coefficient	$\mathrm{mm\,^{\circ}C^{-1}\,d^{-1}}$	3.0
	W_{scale}	Snow cover scale	mm	25.0
	b_{inf}	Infiltration-capacity shape parameter	–	0.2

Each parameter takes a single default value applied uniformly across all grid cells; these defaults follow conventions in established LSMs (e.g., Niu et al., 2011; Lawrence et al., 2019), adjusted for the daily, grid-scale configuration used here.

https://doi.org/10.5194/egusphere-2026-3294
Preprint. Discussion started: 29 July 2026

Table C2. PFT-based prescribed parameters.

Module	Symbol	Parameter
Radiative transfer	SAI	Stem area index
	$\rho_{\Lambda,\mathrm{veg}}$, $\tau_{\Lambda,\mathrm{veg}}$	Leaf and stem reflectance and transmittance (VIS, NIR)
Evapotranspiration	h_c	Canopy height
	d_leaf	Characteristic leaf dimension
Photosynthesis	$\mathrm{PAR}_{1/2}$	Radiation half-saturation
	k_vpd	VPD sensitivity
Soil hydraulics	β	Root distribution shape parameter
	$\psi_\mathrm{leaf,min}$	Minimum leaf water potential

Each parameter is obtained as a plant-functional-type-fraction-weighted average of per-PFT values from lookup tables, so that it varies with the vegetation composition of each grid cell.

Table C3. Derived soil hydraulic parameters

Symbol	Parameter	Unit
$\theta_{\mathrm{sat},i}$	Saturated volumetric moisture content	$\mathrm{m^3\,m^{-3}}$
$\theta_{\mathrm{fc},i}$	Field-capacity volumetric moisture content	$\mathrm{m^3\,m^{-3}}$
$\theta_{\mathrm{wp},i}$	Wilting-point volumetric moisture content	$\mathrm{m^3\,m^{-3}}$
$K_{\mathrm{sat},i}$	Saturated hydraulic conductivity	$\mathrm{mm\,d^{-1}}$
A_i	Soil water retention coefficient	MPa
B_i	Soil water retention exponent	–
$\psi_{\mathrm{e},i}$	Air-entry water potential	MPa

These parameters are computed layer-wise from sand fraction, clay fraction, organic matter, and bulk density using the Saxton–Rawls pedotransfer functions (Saxton and Rawls, 2006).

https://doi.org/10.5194/egusphere-2026-3294
Preprint. Discussion started: 29 July 2026

References

Anderegg, L. D. L., Griffith, D. M., Cavender-Bares, J., Riley, W. J., Berry, J. A., Dawson, T. E., and Still, C. J.: Representing plant diversity in land models: An evolutionary approach to make "Functional Types" more functional, Global Change Biology, 28, 2541–2554, https://doi.org/10.1111/gcb.16040, 2022.

Anderegg, W. R. L., Konings, A. G., Trugman, A. T., Yu, K., Bowling, D. R., Gabbitas, R., Karp, D. S., Pacala, S., Sperry, J. S., Sulman, B. N., and Zenes, N.: Hydraulic diversity of forests regulates ecosystem resilience during drought, Nature, 561, 538–541, https://doi.org/10.1038/s41586-018-0539-7, 2018.

Baghirov, Z., Jung, M., Reichstein, M., Körner, M., and Kraft, B.: H2MV (v1.0): global physically constrained deep learning water cycle model with vegetation, Geoscientific Model Development, 18, 2921–2943, https://doi.org/10.5194/gmd-18-2921-2025, 2025.

Bao, S., Alonso, L., Wang, S., Gensheimer, J., De, R., and Carvalhais, N.: Toward Robust Parameterizations in Ecosystem-Level Photosynthesis Models, Journal of Advances in Modeling Earth Systems, 15, https://doi.org/10.1029/2022ms003464, 2023.

Bastrikov, V., MacBean, N., Bacour, C., Santaren, D., Kuppel, S., and Peylin, P.: Land surface model parameter optimisation using in situ flux data: comparison of gradient-based versus random search algorithms (a case study using ORCHIDEE v1.9.5.2), Geoscientific Model Development, 11, 4739–4754, https://doi.org/10.5194/gmd-11-4739-2018, 2018.

Beck, H. E., van Dijk, A. I. J. M., de Roo, A., Miralles, D. G., McVicar, T. R., Schellekens, J., and Bruijnzeel, L. A.: Global-scale regionalization of hydrologic model parameters, Water Resources Research, 52, 3599–3622, https://doi.org/10.1002/2015wr018247, 2016.

Beck, H. E., Pan, M., Lin, P., Seibert, J., van Dijk, A. I. J. M., and Wood, E. F.: Global Fully Distributed Parameter Regionalization Based on Observed Streamflow From 4, 229 Headwater Catchments, Journal of Geophysical Research: Atmospheres, 125, https://doi.org/10.1029/2019jd031485, 2020.

Bernacchi, C. J., Singsaas, E. L., Pimentel, C., Portis Jr, A. R., and Long, S. P.: Improved temperature response functions for models of Rubisco-limited photosynthesis, Plant, Cell & Environment, 24, 253–259, https://doi.org/10.1111/j.1365-3040.2001.00668.x, 2001.

Beven, K.: A manifesto for the equifinality thesis, Journal of Hydrology, 320, 18–36, https://doi.org/10.1016/j.jhydrol.2005.07.007, 2006.

Blougouras, G., Jiang, S., Brenning, A., Migliavacca, M., Slater, L. J., Zhou, J., Kumar, R., Tian, L., Wang, C., and Reichstein, M.: Spatiotemporal dynamics of active root zone storage revealed from hybrid machine learning, https://doi.org/10.22541/essoar.176280049.93675424/v1, 2025.

Blyth, E. M., Arora, V. K., Clark, D. B., Dadson, S. J., De Kauwe, M. G., Lawrence, D. M., Melton, J. R., Pongratz, J., Turton, R. H., Yoshimura, K., and Yuan, H.: Advances in Land Surface Modelling, Current Climate Change Reports, 7, 45–71, https://doi.org/10.1007/s40641-021-00171-5, 2021.

Booth, B. B. B., Jones, C. D., Collins, M., Totterdell, I. J., Cox, P. M., Sitch, S., Huntingford, C., Betts, R. A., Harris, G. R., and Lloyd, J.: High sensitivity of future global warming to land carbon cycle processes, Environmental Research Letters, 7, 024 002, https://doi.org/10.1088/1748-9326/7/2/024002, 2012.

Campbell, G.: Derivation of an angle density function for canopies with ellipsoidal leaf angle distributions, Agricultural and Forest Meteorology, 49, 173–176, https://doi.org/10.1016/0168-1923(90)90030-a, 1990.

Campbell, G. S.: A Simple Method for Determining Unsaturated Conductivity from Moisture Retention Data, Soil Science, 117, 311–314, https://doi.org/10.1097/00010694-197406000-00001, 1974.

https://doi.org/10.5194/egusphere-2026-3294
Preprint. Discussion started: 29 July 2026

Cao, S., Li, M., Zhu, Z., Wang, Z., Zha, J., Zhao, W., Duanmu, Z., Chen, J., Zheng, Y., Chen, Y., Myneni, R. B., and Piao, S.: Spatiotemporally consistent global dataset of the GIMMS leaf area index (GIMMS LAI4g) from 1982 to 2020, Earth System Science Data, 15, 4877–4899, https://doi.org/10.5194/essd-15-4877-2023, 2023.

Chen, M., Qian, Z., Boers, N., Jakeman, A. J., Kettner, A. J., Brandt, M., Kwan, M.-P., Batty, M., Li, W., Zhu, R., Luo, W., Ames, D. P., Barton, C. M., Cuddy, S. M., Koirala, S., Zhang, F., Ratti, C., Liu, J., Zhong, T., Liu, J., Wen, Y., Yue, S., Zhu, Z., Zhang, Z., Sun, Z., Lin, J., Ma, Z., He, Y., Xu, K., Zhang, C., Lin, H., and Lü, G.: Iterative integration of deep learning in hybrid Earth surface system modelling, Nature Reviews Earth & Environment, 4, 568–581, https://doi.org/10.1038/s43017-023-00452-7, 2023.

Choudhury, B. J. and Monteith, J. L.: A four-layer model for the heat budget of homogeneous land surfaces, Quarterly Journal of the Royal Meteorological Society, 114, 373–398, https://doi.org/10.1002/qj.49711448006, 1988.

Collatz, G., Ball, J., Grivet, C., and Berry, J. A.: Physiological and environmental regulation of stomatal conductance, photosynthesis and transpiration: a model that includes a laminar boundary layer, Agricultural and Forest Meteorology, 54, 107–136, https://doi.org/10.1016/0168-1923(91)90002-8, 1991.

Colleoni, F., Huynh, N. N. T., Garambois, P.-A., Jay-Allemand, M., Organde, D., Renard, B., De Fournas, T., El Baz, A., Demargne, J., and Javelle, P.: smash v1.0: a differentiable and regionalizable high-resolution hydrological modeling and data assimilation framework, Geoscientific Model Development, 18, 7003–7034, https://doi.org/10.5194/gmd-18-7003-2025, 2025.

Cranko Page, J., Abramowitz, G., De Kauwe, M. G., and Pitman, A. J.: Are Plant Functional Types Fit for Purpose?, Geophysical Research Letters, 51, https://doi.org/10.1029/2023gl104962, 2023.

Deck, K., Braghiere, R. K., Renchon, A. A., Sloan, J., Bozzola, G., Speer, E., Ben Mackay, J., Reddy, T., Phan, K., Gagné-Landmann, A. L., Li, Y., Yatunin, D., Charbonneau, A., Efrat-Henrici, N., Bach, E., Ma, S., Gentine, P., Frankenberg, C., Bloom, A. A., Wang, Y., Longo, M., and Schneider, T.: ClimaLand: A Land Surface Model Designed to Enable Data-Driven Parameterizations, Journal of Advances in Modeling Earth Systems, 18, https://doi.org/10.1029/2025ms005118, 2026.

Dickinson, R. E.: Land Surface Processes and Climate—Surface Albedos and Energy Balance, p. 305–353, Elsevier, ISBN 9780120188253, https://doi.org/10.1016/s0065-2687(08)60176-4, 1983.

Drought 2018 Team and ICOS Ecosystem Thematic Centre: Drought-2018 ecosystem eddy covariance flux product for 52 stations in FLUXNET-Archive format, https://doi.org/10.18160/YVR0-4898, 2020.

ElGhawi, R., Kraft, B., Reimers, C., Reichstein, M., Körner, M., Gentine, P., and Winkler, A. J.: Hybrid modeling of evapotranspiration: inferring stomatal and aerodynamic resistances using combined physics-based and machine learning, Environmental Research Letters, 18, 034 039, https://doi.org/10.1088/1748-9326/acbbe0, 2023.

ElGhawi, R., Reimers, C., Schnur, R., Reichstein, M., Körner, M., Carvalhais, N., and Winkler, A. J.: Hybrid-Modeling of Land-Atmosphere Fluxes Using Integrated Machine Learning in the ICON-ESM Modeling Framework, Journal of Advances in Modeling Earth Systems, 17, https://doi.org/10.1029/2025ms005102, 2025.

Entekhabi, D., Njoku, E. G., O'Neill, P. E., Kellogg, K. H., Crow, W. T., Edelstein, W. N., Entin, J. K., Goodman, S. D., Jackson, T. J., Johnson, J., Kimball, J., Piepmeier, J. R., Koster, R. D., Martin, N., McDonald, K. C., Moghaddam, M., Moran, S., Reichle, R., Shi, J. C., Spencer, M. W., Thurman, S. W., Tsang, L., and Van Zyl, J.: The Soil Moisture Active Passive (SMAP) Mission, Proceedings of the IEEE, 98, 704–716, https://doi.org/10.1109/jproc.2010.2043918, 2010.

Fang, J. and Gentine, P.: Exploring Optimal Complexity for Water Stress Representation in Terrestrial Carbon Models: A Hybrid-Machine Learning Model Approach, Journal of Advances in Modeling Earth Systems, 16, https://doi.org/10.1029/2024ms004308, 2024.

https://doi.org/10.5194/egusphere-2026-3294
Preprint. Discussion started: 29 July 2026

Fang, J., Bowman, K., Zhao, W., Lian, X., and Gentine, P.: Differentiable land model reveals global environmental controls on latent ecological functions, Nature Communications, https://doi.org/10.1038/s41467-026-73395-4, 2026.

Farquhar, G. D., von Caemmerer, S., and Berry, J. A.: A biochemical model of photosynthetic CO2 assimilation in leaves of C3 species, Planta, 149, 78–90, https://doi.org/10.1007/bf00386231, 1980.

Feigl, M., Thober, S., Schweppe, R., Herrnegger, M., Samaniego, L., and Schulz, K.: Automatic Regionalization of Model Parameters for Hydrological Models, Water Resources Research, 58, https://doi.org/10.1029/2022wr031966, 2022.

Felton, A. J., Fisher, J. B., Hufkens, K., Purdy, A. J., Spawn-Lee, S. A., Duloisy, L. F., and Goldsmith, G. R.: Global estimates of the storage and transit time of water through vegetation, Nature Water, 3, 59–69, https://doi.org/10.1038/s44221-024-00365-9, 2025.

Feng, D., Liu, J., Lawson, K., and Shen, C.: Differentiable, Learnable, Regionalized Process-Based Models With Multiphysical Outputs can Approach State-Of-The-Art Hydrologic Prediction Accuracy, Water Resources Research, 58, https://doi.org/10.1029/2022wr032404, 2022.

Fisher, J. B., Lee, B., Purdy, A. J., Halverson, G. H., Dohlen, M. B., Cawse-Nicholson, K., Wang, A., Anderson, R. G., Aragon, B., Arain, M. A., Baldocchi, D. D., Baker, J. M., Barral, H., Bernacchi, C. J., Bernhofer, C., Biraud, S. C., Bohrer, G., Brunsell, N., Cappelaere, B., Castro-Contreras, S., Chun, J., Conrad, B. J., Cremonese, E., Demarty, J., Desai, A. R., De Ligne, A., Foltýnová, L., Goulden, M. L., Griffis, T. J., Grünwald, T., Johnson, M. S., Kang, M., Kelbe, D., Kowalska, N., Lim, J., Maïnassara, I., McCabe, M. F., Missik, J. E., Mohanty, B. P., Moore, C. E., Morillas, L., Morrison, R., Munger, J. W., Posse, G., Richardson, A. D., Russell, E. S., Ryu, Y., Sanchez-Azofeifa, A., Schmidt, M., Schwartz, E., Sharp, I., Šigut, L., Tang, Y., Hulley, G., Anderson, M., Hain, C., French, A., Wood, E., and Hook, S.: ECOSTRESS: NASA's Next Generation Mission to Measure Evapotranspiration From the International Space Station, Water Resources Research, 56, https://doi.org/10.1029/2019wr026058, 2020.

Fisher, R. A. and Koven, C. D.: Perspectives on the Future of Land Surface Models and the Challenges of Representing Complex Terrestrial Systems, Journal of Advances in Modeling Earth Systems, 12, https://doi.org/10.1029/2018ms001453, 2020.

Fisher, R. A., Wieder, W. R., Sanderson, B. M., Koven, C. D., Oleson, K. W., Xu, C., Fisher, J. B., Shi, M., Walker, A. P., and Lawrence, D. M.: Parametric Controls on Vegetation Responses to Biogeochemical Forcing in the CLM5, Journal of Advances in Modeling Earth Systems, 11, 2879–2895, https://doi.org/10.1029/2019ms001609, 2019.

Gelbrecht, M., White, A., Bathiany, S., and Boers, N.: Differentiable programming for Earth system modeling, Geoscientific Model Development, 16, 3123–3135, https://doi.org/10.5194/gmd-16-3123-2023, 2023.

Harper, K. L., Lamarche, C., Hartley, A., Peylin, P., Ottlé, C., Bastrikov, V., San Martín, R., Bohnenstengel, S. I., Kirches, G., Boettcher, M., Shevchuk, R., Brockmann, C., and Defourny, P.: A 29-year time series of annual 300 m resolution plant-functional-type maps for climate models, Earth System Science Data, 15, 1465–1499, https://doi.org/10.5194/essd-15-1465-2023, 2023.

Heuvelmans, G., Muys, B., and Feyen, J.: Regionalisation of the parameters of a hydrological model: Comparison of linear regression models with artificial neural nets, Journal of Hydrology, 319, 245–265, https://doi.org/10.1016/j.jhydrol.2005.07.030, 2006.

Holtzman, N. M., Anderegg, L. D. L., Kraatz, S., Mavrovic, A., Sonnentag, O., Pappas, C., Cosh, M. H., Langlois, A., Lakhankar, T., Tesser, D., Steiner, N., Colliander, A., Roy, A., and Konings, A. G.: L-band vegetation optical depth as an indicator of plant water potential in a temperate deciduous forest stand, Biogeosciences, 18, 739–753, https://doi.org/10.5194/bg-18-739-2021, 2021.

Jackson, R. B., Canadell, J., Ehleringer, J. R., Mooney, H. A., Sala, O. E., and Schulze, E. D.: A global analysis of root distributions for terrestrial biomes, Oecologia, 108, 389–411, https://doi.org/10.1007/bf00333714, 1996.

Jarvis, P. G.: The interpretation of the variations in leaf water potential and stomatal conductance found in canopies in the field, Philosophical Transactions of the Royal Society of London. B, Biological Sciences, 273, 593–610, https://doi.org/10.1098/rstb.1976.0035, 1976.

https://doi.org/10.5194/egusphere-2026-3294
Preprint. Discussion started: 29 July 2026

Jiang, P., Kidger, P., Bandai, T., Baldocchi, D., Liu, H., Xiao, Y., Zhang, Q., Wang, C. T., Steefel, C., and Chen, X.: JAX-CanVeg: A Differentiable Land Surface Model, Water Resources Research, 61, https://doi.org/10.1029/2024wr038116, 2025.

Jiang, S.: ADELM: a differentiable ecohydrological land model, https://doi.org/10.5281/zenodo.20574230, 2026.

Jiang, S., Zheng, Y., and Solomatine, D.: Improving AI System Awareness of Geoscience Knowledge: Symbiotic Integration of Physical Approaches and Deep Learning, Geophysical Research Letters, 47, https://doi.org/10.1029/2020gl088229, 2020.

Jiang, S., Sweet, L., Blougouras, G., Brenning, A., Li, W., Reichstein, M., Denzler, J., Shangguan, W., Yu, G., Huang, F., and Zscheischler, J.: How Interpretable Machine Learning Can Benefit Process Understanding in the Geosciences, Earth's Future, 12, https://doi.org/10.1029/2024ef004540, 2024.

Kaminski, T. and Mathieu, P.-P.: Reviews and syntheses: Flying the satellite into your model: on the role of observation operators in constraining models of the Earth system and the carbon cycle, Biogeosciences, 14, 2343–2357, https://doi.org/10.5194/bg-14-2343-2017, 2017.

Keetz, L. T., Aalstad, K., Fisher, R. A., Poppe Terán, C., Naz, B., Pirk, N., Yilmaz, Y. A., and Skarpaas, O.: Inferring Parameters in a Complex Land Surface Model by Combining Data Assimilation and Machine Learning, Journal of Advances in Modeling Earth Systems, 17, https://doi.org/10.1029/2024ms004542, 2025.

Kerr, Y. H., Waldteufel, P., Wigneron, J.-P., Delwart, S., Cabot, F., Boutin, J., Escorihuela, M.-J., Font, J., Reul, N., Gruhier, C., Juglea, S. E., Drinkwater, M. R., Hahne, A., Martín-Neira, M., and Mecklenburg, S.: The SMOS Mission: New Tool for Monitoring Key Elements ofthe Global Water Cycle, Proceedings of the IEEE, 98, 666–687, https://doi.org/10.1109/jproc.2010.2043032, 2010.

Kingma, D. P. and Ba, J.: Adam: A Method for Stochastic Optimization, https://doi.org/10.48550/ARXIV.1412.6980, 2014.

Knauer, J., El-Madany, T. S., Zaehle, S., and Migliavacca, M.: Bigleaf—An R package for the calculation of physical and physiological ecosystem properties from eddy covariance data, PLOS ONE, 13, e0201 114, https://doi.org/10.1371/journal.pone.0201114, 2018.

Konings, A. G., Holtzman, N. M., Rao, K., Xu, L., and Saatchi, S. S.: Interannual Variations of Vegetation Optical Depth are Due to Both Water Stress and Biomass Changes, Geophysical Research Letters, 48, https://doi.org/10.1029/2021gl095267, 2021.

Koppa, A., Rains, D., Hulsman, P., Poyatos, R., and Miralles, D. G.: A deep learning-based hybrid model of global terrestrial evaporation, Nature Communications, 13, https://doi.org/10.1038/s41467-022-29543-7, 2022.

Kraft, B., Jung, M., Körner, M., Koirala, S., and Reichstein, M.: Towards hybrid modeling of the global hydrological cycle, Hydrology and Earth System Sciences, 26, 1579–1614, https://doi.org/10.5194/hess-26-1579-2022, 2022.

Kumar, S., Kolassa, J., Reichle, R., Crow, W., de Lannoy, G., de Rosnay, P., MacBean, N., Girotto, M., Fox, A., Quaife, T., Draper, C., Forman, B., Balsamo, G., Steele-Dunne, S., Albergel, C., Bonan, B., Calvet, J., Dong, J., Liddy, H., and Ruston, B.: An Agenda for Land Data Assimilation Priorities: Realizing the Promise of Terrestrial Water, Energy, and Vegetation Observations From Space, Journal of Advances in Modeling Earth Systems, 14, https://doi.org/10.1029/2022ms003259, 2022.

Kuppel, S., Peylin, P., Chevallier, F., Bacour, C., Maignan, F., and Richardson, A. D.: Constraining a global ecosystem model with multi-site eddy-covariance data, Biogeosciences, 9, 3757–3776, https://doi.org/10.5194/bg-9-3757-2012, 2012.

Lawrence, D. M., Fisher, R. A., Koven, C. D., Oleson, K. W., Swenson, S. C., Bonan, G., Collier, N., Ghimire, B., van Kampenhout, L., Kennedy, D., Kluzek, E., Lawrence, P. J., Li, F., Li, H., Lombardozzi, D., Riley, W. J., Sacks, W. J., Shi, M., Vertenstein, M., Wieder, W. R., Xu, C., Ali, A. A., Badger, A. M., Bisht, G., van den Broeke, M., Brunke, M. A., Burns, S. P., Buzan, J., Clark, M., Craig, A., Dahlin, K., Drewniak, B., Fisher, J. B., Flanner, M., Fox, A. M., Gentine, P., Hoffman, F., Keppel-Aleks, G., Knox, R., Kumar, S., Lenaerts, J., Leung, L. R., Lipscomb, W. H., Lu, Y., Pandey, A., Pelletier, J. D., Perket, J., Randerson, J. T., Ricciuto, D. M., Sanderson, B. M., Slater, A., Subin, Z. M., Tang, J., Thomas, R. Q., Val Martin, M., and Zeng, X.: The Community Land Model Version 5: Description

https://doi.org/10.5194/egusphere-2026-3294
Preprint. Discussion started: 29 July 2026

of New Features, Benchmarking, and Impact of Forcing Uncertainty, Journal of Advances in Modeling Earth Systems, 11, 4245–4287, https://doi.org/10.1029/2018ms001583, 2019.

Li, X. and Xiao, J.: A Global, 0.05-Degree Product of Solar-Induced Chlorophyll Fluorescence Derived from OCO-2, MODIS, and Reanalysis Data, Remote Sensing, 11, 517, https://doi.org/10.3390/rs11050517, 2019.

Liang, X., Lettenmaier, D. P., Wood, E. F., and Burges, S. J.: A simple hydrologically based model of land surface water and energy fluxes for general circulation models, Journal of Geophysical Research: Atmospheres, 99, 14 415–14 428, https://doi.org/10.1029/94jd00483, 1994.

Linke, S., Lehner, B., Ouellet Dallaire, C., Ariwi, J., Grill, G., Anand, M., Beames, P., Burchard-Levine, V., Maxwell, S., Moidu, H., Tan, F., and Thieme, M.: Global hydro-environmental sub-basin and river reach characteristics at high spatial resolution, Scientific Data, 6, https://doi.org/10.1038/s41597-019-0300-6, 2019.

Liu, Y., Flournoy, O., Zhang, Q., Novick, K. A., Koster, R. D., and Konings, A. G.: Canopy Height and Climate Dryness Parsimoniously Explain Spatial Variation of Unstressed Stomatal Conductance, Geophysical Research Letters, 49, https://doi.org/10.1029/2022gl099339, 2022.

MacBean, N., Bacour, C., Raoult, N., Bastrikov, V., Koffi, E. N., Kuppel, S., Maignan, F., Ottlé, C., Peaucelle, M., Santaren, D., and Peylin, P.: Quantifying and Reducing Uncertainty in Global Carbon Cycle Predictions: Lessons and Perspectives From 15 Years of Data Assimilation Studies With the ORCHIDEE Terrestrial Biosphere Model, Global Biogeochemical Cycles, 36, https://doi.org/10.1029/2021gb007177, 2022.

Margiotta, E. R., Kennedy, D., Hawkins, L. R., and Trugman, A. T.: Functional Diversity in Land Surface Modeling: Where and When Does It Matter for the Terrestrial Carbon Cycle?, Global Change Biology, 32, https://doi.org/10.1111/gcb.70785, 2026.

Massoud, E. C., Xu, C., Fisher, R. A., Knox, R. G., Walker, A. P., Serbin, S. P., Christoffersen, B. O., Holm, J. A., Kueppers, L. M., Ricciuto, D. M., Wei, L., Johnson, D. J., Chambers, J. Q., Koven, C. D., McDowell, N. G., and Vrugt, J. A.: Identification of key parameters controlling demographically structured vegetation dynamics in a land surface model: CLM4.5(FATES), Geoscientific Model Development, 12, 4133–4164, https://doi.org/10.5194/gmd-12-4133-2019, 2019.

Merz, R. and Blöschl, G.: Regionalisation of catchment model parameters, Journal of Hydrology, 287, 95–123, https://doi.org/10.1016/j.jhydrol.2003.09.028, 2004.

Miralles, D. G., Bonte, O., Koppa, A., Baez-Villanueva, O. M., Tronquo, E., Zhong, F., Beck, H. E., Hulsman, P., Dorigo, W., Verhoest, N. E. C., and Haghdoost, S.: GLEAM4: global land evaporation and soil moisture dataset at 0.1° resolution from 1980 to near present, Scientific Data, 12, https://doi.org/10.1038/s41597-025-04610-y, 2025.

Monteith, J.: Evaporation and environment., in: Symposia of the Society for Experimental Biology, vol. 19, pp. 205–234, 1965.

Muñoz-Sabater, J., Dutra, E., Agustí-Panareda, A., Albergel, C., Arduini, G., Balsamo, G., Boussetta, S., Choulga, M., Harrigan, S., Hersbach, H., Martens, B., Miralles, D. G., Piles, M., Rodríguez-Fernández, N. J., Zsoter, E., Buontempo, C., and Thépaut, J.-N.: ERA5-Land: a state-of-the-art global reanalysis dataset for land applications, Earth System Science Data, 13, 4349–4383, https://doi.org/10.5194/essd-13-4349-2021, 2021.

Nash, J. and Sutcliffe, J.: River flow forecasting through conceptual models part I — A discussion of principles, Journal of Hydrology, 10, 282–290, https://doi.org/10.1016/0022-1694(70)90255-6, 1970.

Nelson, J. A., Walther, S., Gans, F., Kraft, B., Weber, U., Novick, K., Buchmann, N., Migliavacca, M., Wohlfahrt, G., Šigut, L., Ibrom, A., Papale, D., Göckede, M., Duveiller, G., Knohl, A., Hörtnagl, L., Scott, R. L., Dušek, J., Zhang, W., Hamdi, Z. M., Reichstein, M., Aranda-Barranco, S., Ardö, J., Op de Beeck, M., Billesbach, D., Bowling, D., Bracho, R., Brümmer, C., Camps-Valls, G., Chen, S., Cleverly, J. R., Desai, A., Dong, G., El-Madany, T. S., Euskirchen, E. S., Feigenwinter, I., Galvagno, M., Gerosa, G. A., Gielen, B., Goded, I., Goslee, S., Gough, C. M., Heinesch, B., Ichii, K., Jackowicz-Korczynski, M. A., Klosterhalfen, A., Knox, S., Kobayashi, H., Kohonen, K.-M., Korkiakoski, M., Mammarella, I., Gharun, M., Marzuoli, R., Matamala, R., Metzger, S., Montagnani, L., Nicolini, G., O'Halloran, T., Ourcival, J.-M., Peichl, M., Pendall, E., Ruiz Reverter, B., Roland, M., Sabbatini, S., Sachs, T., Schmidt, M., Schwalm, C. R., Shekhar, A., Silberstein, R., Silveira, M. L., Spano, D., Tagesson, T., Tramontana, G., Trotta, C., Turco, F., Vesala, T., Vincke, C., Vitale, D., Vivoni, E. R., Wang, Y., Woodgate, W., Yepez, E. A., Zhang, J., Zona, D., and Jung, M.: X-BASE: the first terrestrial carbon and water flux products from an extended data-driven scaling framework, FLUXCOM-X, Biogeosciences, 21, 5079–5115, https://doi.org/10.5194/bg-21-5079-2024, 2024.

Niu, G.-Y., Yang, Z.-L., Mitchell, K. E., Chen, F., Ek, M. B., Barlage, M., Kumar, A., Manning, K., Niyogi, D., Rosero, E., Tewari, M., and Xia, Y.: The community Noah land surface model with multiparameterization options (Noah-MP): 1. Model description and evaluation with local-scale measurements, Journal of Geophysical Research, 116, https://doi.org/10.1029/2010jd015139, 2011.

Parajka, J., Merz, R., and Blöschl, G.: A comparison of regionalisation methods for catchment model parameters, Hydrology and Earth System Sciences, 9, 157–171, https://doi.org/10.5194/hess-9-157-2005, 2005.

Paschalis, A., Bonetti, S., Guo, Y., and Fatichi, S.: On the Uncertainty Induced by Pedotransfer Functions in Terrestrial Biosphere Modeling, Water Resources Research, 58, https://doi.org/10.1029/2021wr031871, 2022.

Paszke, A., Gross, S., Massa, F., Lerer, A., Bradbury, J., Chanan, G., Killeen, T., Lin, Z., Gimelshein, N., Antiga, L., Desmaison, A., Köpf, A., Yang, E., DeVito, Z., Raison, M., Tejani, A., Chilamkurthy, S., Steiner, B., Fang, L., Bai, J., and Chintala, S.: PyTorch: An Imperative Style, High-Performance Deep Learning Library, https://doi.org/10.48550/ARXIV.1912.01703, 2019.

Poggio, L., de Sousa, L. M., Batjes, N. H., Heuvelink, G. B. M., Kempen, B., Ribeiro, E., and Rossiter, D.: SoilGrids 2.0: producing soil information for the globe with quantified spatial uncertainty, SOIL, 7, 217–240, https://doi.org/10.5194/soil-7-217-2021, 2021.

Raoult, N., Douglas, N., MacBean, N., Kolassa, J., Quaife, T., Roberts, A. G., Fisher, R., Fer, I., Bacour, C., Dagon, K., Hawkins, L., Carvalhais, N., Cooper, E., Dietze, M. C., Gentine, P., Kaminski, T., Kennedy, D., Liddy, H. M., Moore, D. J. P., Peylin, P., Pinnington, E., Sanderson, B., Scholze, M., Seiler, C., Smallman, T. L., Vergopolan, N., Viskari, T., Williams, M., and Zobitz, J.: Parameter Estimation in Land Surface Models: Challenges and Opportunities With Data Assimilation and Machine Learning, Journal of Advances in Modeling Earth Systems, 17, https://doi.org/10.1029/2024ms004733, 2025.

Reichstein, M., Camps-Valls, G., Stevens, B., Jung, M., Denzler, J., Carvalhais, N., and Prabhat: Deep learning and process understanding for data-driven Earth system science, Nature, 566, 195–204, https://doi.org/10.1038/s41586-019-0912-1, 2019.

Samaniego, L., Kumar, R., and Attinger, S.: Multiscale parameter regionalization of a grid-based hydrologic model at the mesoscale, Water Resources Research, 46, https://doi.org/10.1029/2008wr007327, 2010.

Saxton, K. E. and Rawls, W. J.: Soil Water Characteristic Estimates by Texture and Organic Matter for Hydrologic Solutions, Soil Science Society of America Journal, 70, 1569–1578, https://doi.org/10.2136/sssaj2005.0117, 2006.

Sellers, P., Berry, J., Collatz, G., Field, C., and Hall, F.: Canopy reflectance, photosynthesis, and transpiration. III. A reanalysis using improved leaf models and a new canopy integration scheme., Remote Sensing of Environment, 42, 187–216, https://doi.org/10.1016/0034-4257(92)90102-p, 1992.

Sellers, P. J.: Canopy reflectance, photosynthesis and transpiration, International Journal of Remote Sensing, 6, 1335–1372, https://doi.org/10.1080/01431168508948283, 1985.

Sellers, P. J., Randall, D. A., Collatz, G. J., Berry, J. A., Field, C. B., Dazlich, D. A., Zhang, C., Collelo, G. D., and Bounoua, L.: A revised land surface parameterization (SiB2) for atmospheric GCMs. Part I: Model formulation, Journal of Climate, 9, 676–705, https://doi.org/10.1175/1520-0442(1996)009<0676:ARLSPF>2.0.CO;2, 1996.

Shen, C., Appling, A. P., Gentine, P., Bandai, T., Gupta, H., Tartakovsky, A., Baity-Jesi, M., Fenicia, F., Kifer, D., Li, L., Liu, X., Ren, W., Zheng, Y., Harman, C. J., Clark, M., Farthing, M., Feng, D., Kumar, P., Aboelyazeed, D., Rahmani, F., Song, Y., Beck, H. E., Bindas, T., Dwivedi, D., Fang, K., Höge, M., Rackauckas, C., Mohanty, B., Roy, T., Xu, C., and Lawson, K.: Differentiable modelling to unify machine learning and physical models for geosciences, Nature Reviews Earth & Environment, 4, 552–567, https://doi.org/10.1038/s43017-023-00450-9, 2023.

Tang, G., Wood, A. W., and Swenson, S.: On Using AI-Based Large-Sample Emulators for Land/Hydrology Model Calibration and Regionalization, Water Resources Research, 61, https://doi.org/10.1029/2024wr039525, 2025.

Tian, W., Yu, H., Zhao, S., Cao, Y., Yi, W., Xu, J., and Nan, Z.: NoahPy: a differentiable Noah land surface model for simulating permafrost thermo-hydrology, Geoscientific Model Development, 19, 57–72, https://doi.org/10.5194/gmd-19-57-2026, 2026.

Torres-Ruiz, J. M., Cochard, H., Delzon, S., Boivin, T., Burlett, R., Cailleret, M., Corso, D., Delmas, C. E. L., De Caceres, M., Diaz-Espejo, A., Fernández-Conradi, P., Guillemot, J., Lamarque, L. J., Limousin, J., Mantova, M., Mencuccini, M., Morin, X., Pimont, F., De Dios, V. R., Ruffault, J., Trueba, S., and Martin-StPaul, N. K.: Plant hydraulics at the heart of plant, crops and ecosystem functions in the face of climate change, New Phytologist, 241, 984–999, https://doi.org/10.1111/nph.19463, 2023.

Tsai, W.-P., Feng, D., Pan, M., Beck, H., Lawson, K., Yang, Y., Liu, J., and Shen, C.: From calibration to parameter learning: Harnessing the scaling effects of big data in geoscientific modeling, Nature Communications, 12, https://doi.org/10.1038/s41467-021-26107-z, 2021.

Ukkola, A. M., Haughton, N., De Kauwe, M. G., Abramowitz, G., and Pitman, A. J.: FluxnetLSM R package (v1.0): a community tool for processing FLUXNET data for use in land surface modelling, Geoscientific Model Development, 10, 3379–3390, https://doi.org/10.5194/gmd-10-3379-2017, 2017.

Ukkola, A. M., Abramowitz, G., and De Kauwe, M. G.: A flux tower dataset tailored for land model evaluation, Earth System Science Data, 14, 449–461, https://doi.org/10.5194/essd-14-449-2022, 2022.

Van Looy, K., Bouma, J., Herbst, M., Koestel, J., Minasny, B., Mishra, U., Montzka, C., Nemes, A., Pachepsky, Y. A., Padarian, J., Schaap, M. G., Tóth, B., Verhoef, A., Vanderborght, J., van der Ploeg, M. J., Weihermüller, L., Zacharias, S., Zhang, Y., and Vereecken, H.: Pedotransfer Functions in Earth System Science: Challenges and Perspectives, Reviews of Geophysics, 55, 1199–1256, https://doi.org/10.1002/2017rg000581, 2017.

Verhoef, A., Zeng, Y., Agam, N., Best, M., Bonetti, S., Boussetta, S., Chaney, N., Cuntz, M., Edwards, J., Gupta, S., Heitman, J., Huang, M., Jarvis, N., Jiang, S., Kandala, R., Kiałka, F., Lian, T., Mu, M., Nemes, A., Paulus, S. J., Raoult, N., Reddy, K. N., Romano, N., Sabot, M., Vanderborght, J., van der Ploeg, M., van Oevelen, P., Wang, Y., Wang, Y., Weber, T. K. D., Marthews, T., and Weihermüller, L.: Rethinking Soils in Land Surface Models, Bulletin of the American Meteorological Society, 107, E665–E674, https://doi.org/10.1175/bams-d-26-0003.1, 2026.

Wang, C., Jiang, S., Zheng, Y., Han, F., Kumar, R., Rakovec, O., and Li, S.: Distributed Hydrological Modeling With Physics-Encoded Deep Learning: A General Framework and Its Application in the Amazon, Water Resources Research, 60, https://doi.org/10.1029/2023wr036170, 2024.

Warm Winter 2020 Team and ICOS Ecosystem Thematic Centre: Warm Winter 2020 ecosystem eddy covariance flux product for 73 stations in FLUXNET-Archive format—release 2022-1, https://doi.org/10.18160/2G60-ZHAK, 2020.

Weber, T. K. D., Weihermüller, L., Nemes, A., Bechtold, M., Degré, A., Diamantopoulos, E., Fatichi, S., Filipović, V., Gupta, S., Hohenbrink, T. L., Hirmas, D. R., Jackisch, C., de Jong van Lier, Q., Koestel, J., Lehmann, P., Marthews, T. R., Minasny, B., Pagel, H., van der Ploeg, M., Shojaeezadeh, S. A., Svane, S. F., Szabó, B., Vereecken, H., Verhoef, A., Young, M., Zeng, Y., Zhang, Y., and

https://doi.org/10.5194/egusphere-2026-3294
Preprint. Discussion started: 29 July 2026

Bonetti, S.: Hydro-pedotransfer functions: a roadmap for future development, Hydrology and Earth System Sciences, 28, 3391–3433, https://doi.org/10.5194/hess-28-3391-2024, 2024.

Zhang, B., Kang, S., Li, F., and Zhang, L.: Comparison of three evapotranspiration models to Bowen ratio-energy balance method for a vineyard in an arid desert region of northwest China, Agricultural and Forest Meteorology, 148, 1629–1640, https://doi.org/10.1016/j.agrformet.2008.05.016, 2008.